Quasi-periodic Time-spectral Methods for Flutter and Gust Response

Nathan L. Mundis * Dimitri J. Mavriplis † Jay Sitaraman ‡
Department of Mechanical Engineering, University of Wyoming, Laramie, Wyoming 82071-3295

Periodic and quasi-periodic time-spectral methods are applied to the demanding problems of aeroelastic flutter and gust response. Both a standard time-implicit method and a quasi-periodic time-spectral method are developed that take into account the coupling among the three fundamental aspects of computational aeroelastic calculations: unsteady flow equations, time dependent structural response to aerodynamic loads, and moving meshes. Results from the time-implicit and time-spectral methods are then compared in order to demonstrate the capability of time-spectral methods to solve aeroelastic and gust response problems. Results from many different coupled fluid/structure problems are presented for two-dimensional representations of both fixed-wing and rotary-wing aeroelastic response both with and without gusts of different lengths. It is shown that time-spectral based methods can be used to solve every reasonable combination of airfoil motion and gust response that has thus far been attempted, as presented in the current work.

Introduction

The time-spectral method, based on the use of discrete Fourier analysis, is similar to the harmonic balance method, developed by Hall (Ref. 1) and McMullen (Refs. 2,3), which transforms the unsteady equations in the physical domain to a set of steady equations in the frequency domain. Gopinath (Refs. 4, 5) proposed to solve the time-spectral equations, not in the frequency domain, but directly in the time domain, by applying the time-spectral discretization operator, which transforms the continuous time signal into a specified number of discrete time instances by first applying the discrete Fourier transform to the continuous time signal and then the inverse, discrete Fourier transform to the resultant harmonic spectrum. The time-spectral method has been shown to be faster than the dual-time stepping implicit methods using backwards difference time formulae for time-periodic, aerodynamic computations, such as turbomachinery flows (Refs. 2, 5), oscillatory pitching airfoil/wing cases (Refs. 4, 6), flapping wing (Ref. 7), helicopter rotor (Refs. 8,9) and vortex shedding problems (Ref. 3).

In the recent past, the time-spectral method has been proven capable of solving the coupled fluid/structure equations for the purely periodic problem of a helicopter rotor in constant speed forward flight (Refs. 8,9). Similarly, the simulation of aeroelastic flutter phenomena is computationally expensive and could benefit tremendously from the successful application of a more efficient time integration scheme. However, time-spectral methods are not directly applicable to most flutter problems since these problems are usually not purely periodic. In previous work, we have introduced a hybrid BDF/time-spectral approach (BDFTS) which aims to simulate quasi-periodic flows with slow transients combined with relatively fast periodic content using global BDF time step sizes of the order of the period length, while making use of the properties of the time-spectral approach to capture accurate details of the periodic flow components (Refs. 10–12). The aeroelastic flutter problem is a coupled fluid/structural problem with strong periodic content, i.e. the pitching and plunging of the airfoil or wing, and a slow transient, i.e. increasing or decreasing amplitude of the periodic motion. These factors, coupled with the abundance of published solutions to aeroelastic flutter problems (Refs. 13–15) make it the ideal motivation for a coupled fluid-structure, quasi-periodic time-spectral method.

Further, extending time-spectral methods to address gust response problems pushes the limits of applicability of these methods since the timescale of the gust can be any length, from a small fraction of the period of blade motion to several periods of blade motion. Previously, quasi-periodic time-spectral methods have only been demonstrated on problems where the transient is on the order of several periods of blade motion, and these methods are not well suited to problems where the transient is less than the period of blade motion. The problems presented in the current work are such that gusts only affect the airfoil section for a fraction of its period of motion and can be solved using purely-periodic time-spectral so long as enough spectral harmonics are present to accurately resolve the gust profile. Note that both aeroelastic flutter and gust response are critical problems in the context of rotorcraft and have been traditionally modeled using lower order lifting-line based aerodynamics (Ref. 16). Herein, we propose a computationally efficient methodology that can utilize the Euler or Navier-Stokes equations to model the aerodynamics.

In the following sections we present the necessary components for solving two-dimensional aeroelastic flutter and gust response problems using time-spectral methods. We first outline the governing equations and the base solver for the aerodynamic component. We then discuss the time-spectral method and subsequently the hybrid BDF/time-spectral approach for the flow solver. Next, we discuss the structural

*Graduate Research Assistant; email: nmundis@uwyo.edu.
†Professor; email: mavripl@uwyo.edu.
‡Assistant Professor; email: jsitaram@uwyo.edu.
Presented at the AHS 69th Annual Forum, Phoenix, Arizona, May 21–23, 2013.

equations and how they are transformed for efficient solution. Subsequently, we discuss some of the details of solving the structural equations simultaneously with the flow equations in the time-spectral approach. Following, the prescription of gusts via the Split Velocity Method is discussed.

In the results sections, first, BDFTS is applied to the important practical problem of aeroelastic flutter, and the results are compared to the time-implicit, second-order backward-difference (BDF2) approach, having been validated previously. Then, the aeroelastic response of an airfoil with a prescribed pitching motion (to simulate the cyclic control input of a rotor) is solved and compared to the time-implicit method. Next, the lift and moment produced by a gust on a rigid airfoil are found and juxtaposed with their corresponding BDF2 solutions. Subsequently, the aeroelastic response of this fixed-wing airfoil model to the prescribed gust is presented. Following, the two previous exercises are repeated for an airfoil with a prescribed pitching input, comparing both the forces produced for rigid motion and the aeroelastic response. Finally, we examine the time-solution accuracy convergence as increasing temporal and harmonic resolution is used.

Theory and Methodology

Flow Equations and Solver

The Euler equations in conservative form can be written as:

$$\frac{\partial \mathbf{U}}{\partial t} + \nabla \cdot (\mathbf{F}(\mathbf{U}) = 0 \tag{1}$$

where $\mathbf{U}$ represents the vector of conserved quantities (mass, momentum, and energy) and $\mathbf{F}(\mathbf{U})$ represents the convective fluxes. Integrating over a (moving) control volume $\Omega(t)$, we obtain:

$$\int_{\Omega(t)} \frac{\partial \mathbf{U}}{\partial t} dV + \int_{\partial\Omega(t)} (\mathbf{F}(\mathbf{U}) \cdot \tilde{\mathbf{n}}) dS = 0 \tag{2}$$

Using the differential identity

$$\frac{\partial}{\partial t} \int_{\Omega(t)} \mathbf{U} dV = \int_{\Omega(t)} \frac{\partial \mathbf{U}}{\partial t} dV + \int_{\partial\Omega(t)} \mathbf{U}(\dot{\mathbf{x}} \cdot \tilde{\mathbf{n}}) dS \tag{3}$$

where $\dot{\mathbf{x}}$ and $\tilde{\mathbf{n}}$ are the velocity and normal of the interface $\partial\Omega(t)$, respectively, equation (2) becomes:

$$\frac{\partial}{\partial t} \int_{\Omega(t)} \mathbf{U} dV + \int_{\partial\Omega(t)} (\mathbf{F}(\mathbf{U}) - \mathbf{U}\dot{\mathbf{x}}) \cdot \tilde{\mathbf{n}} dS = 0 \tag{4}$$

Considering $\mathbf{U}$ as cell averaged quantities, these equations are discretized in space as:

$$\frac{\partial}{\partial t}(V\mathbf{U}) + \mathbf{R}(\mathbf{U}, \dot{\mathbf{x}}(t), \tilde{\mathbf{n}}(t)) = 0 \tag{5}$$

where $\mathbf{R}(\mathbf{U}, \dot{\mathbf{x}}, \tilde{\mathbf{n}}) = \int_{\partial\Omega(t)} (\mathbf{F}(\mathbf{U}) - \dot{\mathbf{x}}\mathbf{U}) \cdot \tilde{\mathbf{n}} dS$ represents the discrete convective fluxes in ALE form and V denotes the control volume. In the discrete form, $\dot{\mathbf{x}}(t)$ and $\tilde{\mathbf{n}}(t)$ now represent the time varying velocities and surface normals of the control-volume boundary faces.

The Euler equations are discretized by a central difference finite-volume scheme with additional matrix-based artificial dissipation on hybrid, two-dimensional meshes, which may include triangles and quadrilaterals. Second-order accuracy is achieved using a two-pass construction of the artificial dissipation operator, which corresponds to an undivided biharmonic operator. A single unifying face-based data-structure is used in the flow solver for all types of elements. For the base solver, the time derivative in equation (5) is discretized using a second-order backwards difference (BDF2) scheme, resulting in a non-linear system to be solved at each time step. The implicit solution is achieved using flexible Generalized Minimal Residual Method algorithm, with block-colored Gauss Seidel preconditioning. This choice of linear solver allows for the efficient solution of both the BDF2 time-implicit method and the BDFTS method using the full, exact Jacobian.

Time Spectral Method: If the flow is periodic in time, the variables $\mathbf{U}$ can be represented by a discrete Fourier series. The discrete Fourier transform of $\mathbf{U}$ in a period of T is given by (Ref. 4)

$$\widehat{\mathbf{U}}_k = \frac{1}{N} \sum_{n=0}^{N-1} \mathbf{U}^n e^{-ik\frac{2\pi}{T}n\Delta t} \tag{6}$$

where N is the number of time intervals and $\Delta t = T/N$. The Fourier inverse transform is then given as

$$\mathbf{U}^n = \sum_{k=-\frac{N}{2}}^{\frac{N}{2}-1} \widehat{\mathbf{U}}_k e^{ik\frac{2\pi}{T}n\Delta t} \tag{7}$$

It should be noted that $\frac{N}{2}$ is an integer division operation. Also note equation (7) corresponds to a collocation approximation, i.e. the function $\mathbf{U}(t)$ is projected into the space spanned by the truncated set of complex exponential (spectral) functions, and the expansion coefficients (in this case the $\widehat{\mathbf{U}}_k$) are determined by requiring $\mathbf{U}(t)$ to be equal to its projection at N discrete locations in time, as given by equations (6) and (7).

Differentiating equation (7) in time, we obtain:

$$\frac{\partial}{\partial t}(\mathbf{U}^n) = \frac{2\pi}{T} \sum_{k=-\frac{N}{2}}^{\frac{N}{2}-1} ik\widehat{\mathbf{U}}_k e^{ik\frac{2\pi}{T}n\Delta t} \tag{8}$$

Substituting equation (6) into equation (8), we get (Refs. 17, 18)

$$\frac{\partial}{\partial t}(\mathbf{U}^n) = \sum_{j=0}^{N-1} d_n^j \mathbf{U}^j \tag{9}$$

where

$$d_n^j = \begin{cases} \frac{2\pi}{T}\frac{1}{2}(-1)^{n-j}\cot(\frac{\pi(n-j)}{N}) & n \neq j \\ 0 & n = j \end{cases} \tag{10}$$

for an even number of time instances and

$$d_n^j = \begin{cases} \frac{2\pi}{T}\frac{1}{2}(-1)^{n-j}\csc(\frac{\pi(n-j)}{N}) & n \neq j \\ 0 & n = j \end{cases} \quad (11)$$

for an odd number of time instances. The collocation approach for solving equation (5) consists of substituting the collocation approximation for the continuous function $\mathbf{U}(t)$ given by equation (7) into equation (5), and requiring equation (5) to hold exactly at the same N discrete locations in time (i.e. multiplying (5) by the dirac delta test function $\delta(t-t^n)$ and integrating over all time), yielding:

$$\sum_{j=0}^{N-1} d_n^j V^j \mathbf{U}^j + \mathbf{R}(\mathbf{U}^n, \dot{\mathbf{x}}^n, \tilde{\mathbf{n}}^n) = 0 \qquad n = 0, 1, ..., N-1 \quad (12)$$

This results in a system of N equations for the N time instances $\mathbf{U}^n$ which are all coupled through the summation over the time instances in the time derivative term. The spatial discretionary operators remain unchanged in the time-spectral approach, with only the requirement that each spatial solution be evaluated at the appropriate temporal location. Thus, the time-spectral method may be implemented without any modifications to an existing spatial discretionary, requiring only the addition of the temporal discretionary coupling term, although the N time instances must be solved simultaneously due to this coupling.

Hybrid BDF/Time Spectral Method: The quasi-periodic time-spectral form is derived through the use of polynomial subtraction for quasi-periodic functions by subtracting out the non-periodic transient, which can be modeled using a polynomial basis set, and approximating the remaining purely periodic component with a spectral basis (Ref. 19). From the point of view of a collocation method, this corresponds to using a mixed spectral/polynomial basis set for the projection of the continuous solution (in the time dimension).

We proceed by splitting the quasi-periodic temporal variation of the solution into a periodic and slowly varying mean flow as:

$$\mathbf{U}(t) = \sum_{k=-\frac{N}{2}}^{\frac{N}{2}-1} \widehat{\mathbf{U}}_k e^{ik\frac{2\pi}{T}n\Delta t} + \bar{\mathbf{U}}(t) \quad (13)$$

where the slowly varying mean flow is approximated by a collocation method using a polynomial basis set as:

$$\bar{\mathbf{U}}(t) = \phi_{12}(t)\mathbf{U}^{m+1} + \phi_{11}(t)\mathbf{U}^m \quad (14)$$

for a linear variation and

$$\bar{\mathbf{U}}(t) = \phi_{23}(t)\mathbf{U}^{m+1} + \phi_{22}(t)\mathbf{U}^m + \phi_{21}(t)\mathbf{U}^{m-1} \quad (15)$$

for a quadratic variation in time. Here $\mathbf{U}^m$ and $\mathbf{U}^{m+1}$ represent discrete solution instances in time usually taken as the beginning and ending points of the considered period in the quasi-periodic motion (and $\mathbf{U}^{m-1}$ corresponds to the beginning point of the previous period). In the first case, $\phi_{12}(t)$ and $\phi_{11}(t)$ correspond to the linear interpolation functions given by:

$$\phi_{11}(t) = \frac{t^{m+1} - t}{T} \quad (16)$$

$$\phi_{12}(t) = \frac{t - t^m}{T} \quad (17)$$

with the period given as $T = t^{m+1} - t^m$. Similarly, the $\phi_{23}(t), \phi_{22}(t), \phi_{21}(t)$ are given by the corresponding quadratic interpolation functions. Note that in this case, the collocation approximation leads to the determination of the Fourier coefficients as:

$$\widehat{\mathbf{U}}_k = \frac{1}{N}\sum_{n=0}^{N-1} \tilde{\mathbf{U}}^n e^{-ik\frac{2\pi}{T}n\Delta t} \quad (18)$$

with $\tilde{\mathbf{U}}^n = \mathbf{U}^n - \bar{\mathbf{U}}^n$ defined as the remaining periodic component of the function after polynomial subtraction. Differentiating equation (13) and making use of equations (9) and (18) we obtain the following expression for the time derivative:

$$\frac{\partial}{\partial t}(\mathbf{U}^n) = \sum_{j=0}^{N-1} d_n^j \tilde{\mathbf{U}}^j + \phi'_{12}(t_n)\mathbf{U}^{m+1} + \phi'_{11}(t_n)\mathbf{U}^m \quad (19)$$

for the case of a linear polynomial functions in time. The $\phi'_{12}(t_n)$ and $\phi'_{11}(t_n)$ represent the time derivatives of the polynomial basis functions (resulting in the constant values $\frac{-1}{T}$ and $\frac{1}{T}$ in this case), and the various time instances are given by:

$$t_j = t_m + \frac{j}{N}(t_{m+1} - t_m), \qquad j = 0, \ldots, N-1$$

We also note that $\bar{\mathbf{U}}(t_m) = \mathbf{U}^m = \mathbf{U}(t_m)$ and thus we have $\tilde{\mathbf{U}}^0 = 0$. In other words, the constant mode in the spectral representation must be taken as zero, since it is contained in the polynomial component of the function representation. Therefore, the $j = 0$ component in the summation can be dropped, and rewriting equation (19) in terms of the original time instances $\mathbf{U}^n$ we obtain:

$$\frac{\partial}{\partial t}(\mathbf{U}^n) = \sum_{j=1}^{N-1} d_n^j \mathbf{U}^j - (\sum_{j=1}^{N-1} d_n^j \phi_{12}(t_j) - \phi'_{12}(t_n))\mathbf{U}^{m+1} - (\sum_{j=1}^{N-1} d_n^j \phi_{11}(t_j) - \phi'_{11}(t_n))\mathbf{U}^m \quad (20)$$

Finally, the above expression for the time derivative is substituted into equation (5) which is then required to hold exactly at time instances $j = 1, 2, ..., N-1$ and $j = N$ (which corresponds to the $m+1$ time instance):

$$\sum_{j=1}^{N-1} d_n^j V^j \mathbf{U}^j - (\sum_{j=1}^{N-1} d_n^j \phi_{12}(t_j) - \phi'_{12}(t_n))V^{m+1}\mathbf{U}^{m+1} - (\sum_{j=1}^{N-1} d_n^j \phi_{11}(t_j) - \phi'_{11}(t_n))V^m\mathbf{U}^m + \mathbf{R}(\mathbf{U^n}, \dot{\mathbf{x}}^{\mathbf{n}}, \tilde{\mathbf{n}}^{\mathbf{n}}) = 0 \quad n = 1, 2, ..., N \quad (21)$$

As previously, we have N coupled equations for the N unknown time instances, although in this case the $j = 0$ time instance which corresponds to the $\mathbf{U}^m$ values are known from the solution of the previous period, while the $j = N$ or $\mathbf{U}^{m+1}$ values are not known, since these are not equal to the $j = 0$ values as they would be in a purely periodic flow. In the case

of vanishing periodic content, summation terms involving the d_n^j coefficients vanish by virtue of equation (19) with $\tilde{\mathbf{U}}^j = 0$ and it is easily verified that the above formulation reduces to a first-order backwards difference scheme with a time step equal to the period T. On the other hand, for purely periodic motion, we have $\mathbf{U}^{m+1} = \mathbf{U}^m$ which results in cancellation of the polynomial derivative terms $\phi'_{12}(t_n)$ and $\phi'_{11}(t_n)$. Furthermore, using the identities $\phi_{12}(t_j) + \phi_{11}(t_j) = 1$, and $\sum_{j=0}^{N-1} d_n^j = 0$, it can be seen that the remaining polynomial terms reduce to the missing $j = 0$ instance in the summation. Given the equality $\mathbf{U}^{m+1} = \mathbf{U}^m$, the last equation at $j = N$ becomes identical to the $j = 0$ equation and the time-spectral method given by equation (12) is recovered.

In this description we have used linear polynomials corresponding to a BDF1 time-stepping scheme for clarity. In practice, BDF2 time-stepping schemes are required for accuracy purposes, and the equivalent scheme based on quadratic polynomials is given as:

$$\begin{aligned}\sum_{j=1}^{N-1} d_n^j V^j \mathbf{U}^j - (\sum_{j=1}^{N-1} d_n^j \phi_{23}(t_j) - \phi'_{23}(t_n)) V^{m+1}\mathbf{U}^{m+1} \\ -(\sum_{j=1}^{N-1} d_n^j \phi_{22}(t_j) - \phi'_{22}(t_n)) V^{m}\mathbf{U}^{m} \\ -(\sum_{j=1}^{N-1} d_n^j \phi_{21}(t_j) - \phi'_{21}(t_n)) V^{m-1}\mathbf{U}^{m-1} \\ +\mathbf{R}(\mathbf{U^n}, \dot{\mathbf{x}}^\mathbf{n}, \tilde{\mathbf{n}}^\mathbf{n}) = 0 \quad n = 1, 2, ..., N\end{aligned} \tag{22}$$

where the values $\mathbf{U}^{m-1}$ and $\mathbf{U}^m$, which correspond to the time instances at the beginning and end of the previous period are known from the solution of earlier periods, and $\mathbf{U}^{m+1} = \mathbf{U}^N$ as previously.

Structural Equations and Solver

The aeroelastic model is based on the response of an airfoil with two degrees of freedom, namely pitch and plunge as shown in Figure (1). The equations of motion for such a system can be summarized as:

$$m\ddot{h} + S_\alpha \ddot{\alpha} + K_h h = -L \tag{23}$$

$$S_\alpha \ddot{h} + I_\alpha \ddot{\alpha} + K_\alpha \alpha = M_{ea} \tag{24}$$

where

m:	mass of airfoil
S_α:	static imbalance
I_α:	sectional moment of inertia of airfoil
K_h:	plunging spring coefficient
K_α:	pitching spring coefficient
h:	vertical displacement (positive downward)
α:	angle-of-attack
L:	sectional lift of airfoil
M_{ea}:	sectional moment of airfoil about elastic axis

Non-dimensionalizing time in equations (23) and (24) by the uncoupled natural frequency of pitch yields:

$$[M]\ddot{\mathbf{q}} + [K]\mathbf{q} = \mathbf{F} \tag{25}$$

where

$$[M] = \begin{bmatrix} 1 & x_\alpha \\ x_\alpha & r_\alpha^2 \end{bmatrix}, \quad [K] = \begin{bmatrix} \left(\frac{\omega_h}{\omega_\alpha}\right)^2 & 0 \\ 0 & r_\alpha^2 \end{bmatrix} \tag{26}$$

are the non-dimensional mass and stiffness matrices. The corresponding non-dimensional load and displacement vectors are:

$$\mathbf{F} = \frac{1}{\pi\mu k_c^2} \begin{bmatrix} -C_l \\ 2C_m \end{bmatrix}, \quad \mathbf{q} = \begin{bmatrix} \frac{h}{b} \\ \alpha \end{bmatrix}, \quad \ddot{\mathbf{q}} = \frac{\partial^2 \mathbf{q}}{\partial \tau^2} \tag{27}$$

where

b:	semichord of airfoil
k_c:	reduced frequency of pitch, $k_c = \frac{\omega_\alpha c}{2U_\infty}$
μ:	airfoil mass ratio, $\mu = \frac{m}{\pi\rho b^2}$
ω_h, ω_α:	uncoupled natural frequencies of plunge and pitch
x_α:	structural parameter defined as $\frac{S_\alpha}{mb}$
r_α^2:	structural parameter defined as $\frac{I_\alpha}{mb}$
C_l, C_m:	section lift coefficient and section moment coefficient about the elastic axis
τ:	structural time, $\tau = \omega_\alpha t$

The reduced frequency k_c is typically written in terms of the flutter velocity V_f as

$$k_c = \frac{\omega_\alpha c}{2U_\infty} = \frac{1}{V_f\sqrt{\mu}} \tag{28}$$

where c is the chord length of the airfoil, U_∞ is the freestream velocity, and the flutter velocity V_f is defined as

$$V_f = \frac{U_\infty}{\omega_\alpha b\sqrt{\mu}} \tag{29}$$

The natural pitch frequency is found by solving equation (29) for ω_α in terms of the prescribed flutter velocity V_f.

Transformation of Structural Equations into First Order Form: The aeroelastic equations as shown in Equation (25) are second-order partial differential equations. A transformation to first-order equations is used in order to facilitate the solution procedure. The transformation used is:

$$\mathbf{r_1} = \mathbf{q} \tag{30}$$

$$\mathbf{r_2} = \dot{\mathbf{r}}_\mathbf{1} \tag{31}$$

The resulting first-order equations are then:

$$\dot{\mathbf{r}}_\mathbf{1} = \mathbf{r_2} \tag{32}$$

$$\dot{\mathbf{r}}_\mathbf{2} = -[M]^{-1}[K]\mathbf{r_1} + [M]^{-1}\mathbf{F} \tag{33}$$

and in matrix notation:

$$\begin{bmatrix} \dot{\mathbf{r}}_\mathbf{1} \\ \dot{\mathbf{r}}_\mathbf{2} \end{bmatrix} + \begin{bmatrix} 0 & -[I] \\ [M]^{-1}[K] & 0 \end{bmatrix} \begin{bmatrix} \mathbf{r_1} \\ \mathbf{r_2} \end{bmatrix} = \begin{bmatrix} 0 \\ [M]^{-1}\mathbf{F} \end{bmatrix} \tag{34}$$

$$\dot{\mathbf{r}} + [\Psi]\mathbf{r} = \Phi \tag{35}$$

The matrix $[\Psi]$ is a constant and can be precomputed and stored for use during the time integration process. The time derivative term $\ddot{\mathbf{r}}$ can be discretized using second-order (or first-order) accurate backward difference formulae similar to the time derivative term in the flow equations, as follows:

$$\frac{3\mathbf{r}^{n+1}-4\mathbf{r}^{n}+\mathbf{r}^{n-1}}{2\Delta\tau} \quad + \quad [\Psi]\mathbf{r}^{n+1}=\Phi \tag{36}$$

Or the time derivative can be discretized using either time-spectral or BDFTS formulae, similar to equation (12) for purely periodic time-spectral:

$$\sum_{j=0}^{N-1} \breve{d}_n^j \mathbf{r}^j + [\Psi]\mathbf{r}^n = \Phi \quad n=0,1,2,...,N-1 \tag{37}$$

The structural equation in second-order BDFTS, analogous to equation (22), is discretized as follows:

$$\begin{aligned}\sum_{j=1}^{N-1} \breve{d}_n^j \mathbf{r}^j - (\sum_{j=1}^{N-1} \breve{d}_n^j \breve{\phi}_{23}(\tau_j) - \breve{\phi}'_{23}(\tau_n))\mathbf{r}^{m+1} \\ -(\sum_{j=1}^{N-1} \breve{d}_n^j \breve{\phi}_{22}(\tau_j) - \breve{\phi}'_{22}(\tau_n))\mathbf{r}^{m} \\ -(\sum_{j=1}^{N-1} \breve{d}_n^j \breve{\phi}_{21}(\tau_j) - \breve{\phi}'_{21}(\tau_n))\mathbf{r}^{m-1} \\ +[\Psi]\mathbf{r}^n = \Phi \quad n=1,2,...,N\end{aligned} \tag{38}$$

It should be noted that the time-step $\Delta\tau$ appearing in the denominator of the discretized version of the structural equations is different from the time-step of the flow equations, and their relation is $\Delta\tau = \omega_\alpha \Delta t$, where Δt is the non-dimensional time-step used for the flow equations. Similarly, the period used to calculate the $\breve{d}_n^j$ and $\breve{\phi}$ in time-spectral and BDFTS is the period in the structural time frame. A breve ($\breve{}$) is placed above all quantities that use structural time for clarity. If, for rotorcraft, one wanted to assume that the torsional stiffness were infinite, the torsional equation would need to be removed from the system and the plunge equation non-dimensionalized in a different way.

Implicitly Coupled Aeroelastic Solver: The fluid and structure equations are coupled together implicitly; thus, for each iteration, fluid and structure residuals are found using either the BDF2 or the TS/BDFTS equations as discussed above. Then a Jacobian is found for the entire fluid/structure system. This Jacobian not only couples the fluid residuals to the flow variables and the structural residuals to the structural variables, but also the fluid residuals to the structural variables and the structural variables to the flow variables. Starting with the flow Jacobian, the coupled Jacobian will have as many additional rows and columns as there are structural variables. Thus, a flow Jacobian that is of size $[[4\times N_c]\times[4\times N_c]]$ where N_c is the number of elements in the computational domain of the flow, would become a $[[4\times N_c+N_s]x[4\times N_c+N_s]]$ matrix for the implicitly coupled fluid/structure system, where N_s is the number of structural variables.

While the above represents the size of the Jacobian if all entries were stored, it should be readily apparent that a matrix of this size could not be stored on modern computers for the sizes of computational meshes that are typically used. Instead, only the non-zero blocks of the Jacobian are stored. The first-order Jacobian is stored as an array of its diagonal blocks, which is $[4\times4\times N_c]$, and an array of it's off-diagonal blocks, which are stored on the faces and is $[2\times4\times4\times N_f]$ where the 2 represents the two sides of each face and N_f is the number of faces. The full second-order Jacobian is not stored explicitly; rather, we enable the evaluation of exact Jacobian-vector products as required at each linear solver iteration by storing three sets of diagonal and off-diagonal blocks, which are then used to assemble Jacobian-vector products.

The changes in the structural residuals with respect to the flow variables occur entirely as the lift and moment coefficients vary with the flow variables:

$$\frac{\partial \mathbf{R_s}}{\partial \mathbf{U}} = f(\frac{\partial C_L}{\partial \mathbf{U}}, \frac{\partial C_m}{\partial \mathbf{U}}) \tag{39}$$

This portion of the Jacobian $\frac{\partial \mathbf{R_s}}{\partial \mathbf{U}}$, above, only has non-zero values in cells which include a face that lies on the surface of the airfoil and only these non-zero values are stored.

The changes in the flow residuals with respect to the structural variables occur as a results of the changing motion of the grid as the structural variables change. That is, the structural variables determine both the grid speeds and the orientation of the face normal vectors:

$$\frac{\partial \mathbf{R_f}}{\partial \mathbf{r}} = f(\frac{\partial \dot{\mathbf{x}}}{\partial \mathbf{r}}, \frac{\partial \tilde{\mathbf{n}}}{\partial \mathbf{r}}) \tag{40}$$

In the present work, mesh motion is achieved by translating and rotating the mesh rigidly. Thus, every face in the mesh changes speed and orientation when the mesh is rotated and translated. Because every face is affected, $\frac{\partial \mathbf{R_f}}{\partial \mathbf{r}}$ has the same size as the diagonal blocks of the first-order Jacobian, $[4\times4\times N_c]$. For three-dimensional, fixed-wing or deforming-blade aeroelastic analysis, where rigid mesh motion is not feasible, a deforming mesh capability would be required. This deforming mesh motion will add additional dependencies on cell volume and face area in the above portion of the coupled Jacobian. Additionally, since all face-normals change orientation when a rigid mesh rotates, the above component of the Jacobian has non-zero values for all cells. This would not necessarily be the case for a deforming mesh. It should also be noted that an additional dependence of the structural residuals on the structural variables is included in this framework. This dependence arises as a result of the grid motion since the coefficient of lift is itself dependent on the orientation of the face normals on the airfoil surface:

$$\frac{\partial \mathbf{R_s}}{\partial \mathbf{r}} = f([\Psi], \frac{\partial C_L}{\partial \tilde{\mathbf{n}}}\frac{\partial \tilde{\mathbf{n}}}{\partial \mathbf{r}}) \tag{41}$$

The preceding portion of the full fluid/structure Jacobian retains its $[4\times4]$ size.

The fully-coupled linear system described in the preceding paragraphs and equations is solved for each iteration using

a flexible Generalized Minimal Residual Method (FGMRES) with Block-Colored Gauss-Seidel (BCGS) preconditioning. The BCGS preconditioner uses the first-order accurate flow Jacobian for simplicity and efficiency, and no preconditioning is done on the structural portion of the Krylov vectors. Each Krylov vector is preconditioned with ten iterations of the BCGS smoother. Additionally, each Krylov vector contains contributions from both the fluid and structure equations, which are found by multiplying $\partial \mathbf{R_f}/\partial \mathbf{U}$, $\partial \mathbf{R_s}/\partial \mathbf{U}$, $\partial \mathbf{R_f}/\partial \mathbf{r}$, and $\partial \mathbf{R_s}/\partial \mathbf{r}$ by the appropriate part of the solution vector. For the time implicit scheme (BDF2), FGMRES solves the coupled fluid/structure system implicitly for each time step.

In the case of time-spectral methods, the Jacobian used within FGMRES also couples all time instances implicitly. The preconditioner is used on each time instance individually to eliminate spatial error only, and uses the first-order Jacobian as mentioned above. The use of FGMRES for time-spectral solutions allows the use of many time instances — and thereby the resolution of higher-harmonic content than in previous work (Refs. 10–12, 20), where the number of time instances had been limited to less than 25, when stationary iterative methods had been used to solve the linear system. Additionally, the use of FGMRES largely eliminates the positive correlation of the number of non-linear iterations needed for convergence to the number of time instances used in the solution. This fact is demonstrated in Figure (2) which shows the convergence of one of the cases presented later in this paper for 21 and 79 time instances. As can be seen, only a few more non-linear iterations are needed for the solution of the greater number of time instances.

Method of Gust Prescription

Split Velocity Method: Second-order unstructured, unadapted CFD methods, with their greatly varying cell sizes, quickly dissipate vortices and gusts. Usually, this is not a problem as the only gust of importance is the one shed by the airfoil itself, which need be preserved only as long as it is affecting the flow around that same airfoil. In our case, however, the preservation of a gust that is prescribed very far forward of the airfoil is paramount. One way to preserve such a gust would be to have a uniformly refined mesh where all cells are very small or one could adapt only the cells that the gust occupies at each time step, and then de-refine them once the gust has moved on. Both these solutions, however, greatly increase computational cost. Instead of refinement, gusts in the present work are prescribed using the Split Velocity Method (SVM) (Refs. 21–25).

To derive SVM, we rewrite the Euler equations as given in equation (1) in terms of the conserved variables $\mathbf{U}$:

$$\frac{\partial}{\partial t}\begin{bmatrix}\rho\\ \rho u\\ \rho v\\ \rho E\end{bmatrix}+\frac{\partial}{\partial x}\begin{bmatrix}\rho u\\ \rho u^2+p\\ \rho uv\\ (\rho E+p)u\end{bmatrix}+\frac{\partial}{\partial y}\begin{bmatrix}\rho v\\ \rho uv\\ \rho v^2+p\\ (\rho E+p)v\end{bmatrix}=0 \tag{42}$$

and the ideal gas equation of state is given as:

$$p=(\gamma-1)\rho(E-\frac{1}{2}(u^2+v^2)) \tag{43}$$

In the SVM, the velocity and energy are decomposed into flow and disturbance components as follows:

$$u=\bar{u}+u_d \quad v=\bar{v}+v_d \quad E=\bar{E}+E_d \tag{44}$$

where $\bar{u}$, $\bar{v}$, and $\bar{E}$ are the flow components and u_d, v_d, and E_d are the prescribed disturbance components, in this case, the gust components. The energy components themselves can be found from the equation of state:

$$E=\frac{p}{\rho(\gamma-1)}+\frac{1}{2}(u^2+v^2)=\left\{\frac{p}{\rho(\gamma-1)}+\frac{1}{2}(\bar{u}^2+\bar{v}^2)\right\}+\left\{(\bar{u}u_d+\bar{v}v_d)+\frac{1}{2}(u_d^2+v_d^2)\right\} \tag{45}$$

where the first component in braces is $\bar{E}$ and the rightmost component in braces is E_d. It should be noted that density and pressure remain unchanged by the prescription of the disturbance quantities. Now, we substitute the decomposed components (44) into the Euler equations (42):

$$\frac{\partial}{\partial t}\begin{bmatrix}\rho\\ \rho(\bar{u}+u_d)\\ \rho(\bar{v}+v_d)\\ \rho(\bar{E}+E_d)\end{bmatrix}+\frac{\partial}{\partial x}\begin{bmatrix}\rho(\bar{u}+u_d)\\ \rho(\bar{u}+u_d)^2+p\\ \rho(\bar{u}+u_d)(\bar{v}+v_d)\\ (\rho(\bar{E}+E_d)+p)(\bar{u}+u_d)\end{bmatrix}+\frac{\partial}{\partial y}\begin{bmatrix}\rho(\bar{v}+v_d)\\ \rho(\bar{u}+u_d)(\bar{v}+v_d)\\ \rho(\bar{v}+v_d)^2+p\\ (\rho(\bar{E}+E_d)+p)(\bar{v}+v_d)\end{bmatrix}=0 \tag{46}$$

We then isolate all the disturbance components as follows:

$$\frac{\partial}{\partial t}\begin{bmatrix}\rho\\ \rho\bar{u}\\ \rho\bar{v}\\ \rho\bar{E}\end{bmatrix}+\frac{\partial}{\partial x}\left\{\begin{bmatrix}\rho\bar{u}\\ \rho\bar{u}^2+p\\ \rho\bar{u}\bar{v}\\ (\rho\bar{E}+p)\bar{u}\end{bmatrix}+\begin{bmatrix}\rho u_d\\ \rho\bar{u}u_d\\ \rho\bar{v}u_d\\ \rho\bar{E}u_d\end{bmatrix}\right\}+\frac{\partial}{\partial y}\left\{\begin{bmatrix}\rho\bar{v}\\ \rho\bar{u}\bar{v}\\ \rho\bar{v}^2+p\\ (\rho\bar{E}+p)\bar{v}\end{bmatrix}+\begin{bmatrix}\rho v_d\\ \rho\bar{u}v_d\\ \rho\bar{v}v_d\\ \rho\bar{E}v_d\end{bmatrix}\right\}+\begin{bmatrix}0\\ s_m(u_d)\\ s_m(v_d)\\ s_e(u_d,v_d)\end{bmatrix}=0 \tag{47}$$

where all of the omitted terms are contained in the source terms in the rightmost vector on the left hand side. These source terms are as follows:

$$\begin{aligned} s_m(\xi) &= \rho\left\{\frac{\partial \xi}{\partial t} + (\bar{u}+u_d)\frac{\partial \xi}{\partial x} + (\bar{v}+v_d)\frac{\partial \xi}{\partial y}\right\} \\ s_e(u_d,v_d) &= \bar{u}s_m(u_d) + \bar{u}s_m(v_d) + p(\tfrac{\partial u_d}{\partial x} + \tfrac{\partial v_d}{\partial v}) \end{aligned} \tag{48}$$

where ξ is either u_d or v_d and the pressure is found using only the flow components as follows:

$$p = (\gamma-1)\rho(\bar{E} - \frac{1}{2}(\bar{u}^2+\bar{v}^2)) \tag{49}$$

With these equations taken as a whole, the disturbance component of energy E_d naturally drops out. If we transform the split-velocity Euler equations into integral form and compare them with equation (4), it becomes apparent that SVM corresponds to the Euler equations in ALE form with the addition of the volume-integrated source terms and an additional grid velocity component as follows:

$$\dot{\mathbf{x}} = -\begin{bmatrix} u_d \\ v_d \end{bmatrix} \tag{50}$$

If the source terms are neglected, SVM corresponds to the Field Velocity Method (Ref. 21), which has been used for disturbance calculations in the past and neglects the effect of the airfoil on the disturbance. The velocities calculated as the flow variables are $\bar{u}$ and $\bar{v}$, so the disturbance velocity must be added to the flow output in order to reflect the correct total velocity. The density and pressure calculated, however, are the true density and pressure.

Prescribed Gusts: All of the gusts prescribed herein are $1-cosine$ vertical gusts. The disturbance velocity for such gusts is prescribed by the following:

$$v_d = \left\{ \begin{array}{ccc} 0 & when & x' < 0 \quad x' > l_g \\ \frac{v_{g,max}}{2}\left[1-\cos\frac{2\pi x'}{l_g}\right] & when & 0 \le x' \le l_g \end{array} \right\} \tag{51}$$

where

$$x' = -x + U_\infty t + x_0 \tag{52}$$

where x_0 is the initial position of the leading edge of the gust. This formula gives that $x' = 0$ is the leading edge of the gust and $x' = l_g$ is the trailing edge of the gust at time t.

Test Case and Results

Code Validation in Previous Works

The BDFTS method for both the aerodynamic and structural equations has been validated in previous works (Refs. 10, 20) and will thus be omitted herein. Additionally, the time-implicit solution of the coupled aerodynamic/structural equations has been discussed and its accuracy confirmed in previous works (Refs. 14, 20). As such, its validation will also be omitted in the present work.

Fixed Wing Flutter Results

The BDFTS flow solver, validated previously, is combined with the aeroelastic structural equations discretized with the BDFTS approach to form a BDFTS aeroelastic solver. The solution process for the BDFTS implementation is as follows: first a purely periodic time-spectral solution is found at the actual frequency of flutter. Then, a single period of first-order BDFTS is solved as the airfoil is allowed to respond aeroelastically. Next, enough additional periods are run using second-order BDFTS to determine if the solution is aeroelastically damped, neutral, or excited (i.e. experiencing flutter). It should be noted that for now, the period of flutter is assumed to be known and prescribed for the BDFTS solutions.

To validate the BDFTS aeroelastic solver the two-dimensional swept wing model exhibiting the transonic dip phenomenon suggested by Isogai (Ref. 26) is chosen as the test case. The structural parameters for this case are:

$$\begin{array}{rl} x_\alpha & = 1.8 \\ r_\alpha^2 & = 3.48 \\ \frac{\omega_h}{\omega_\alpha} & = 1.0 \\ \mu & = 60 \\ a & = -2.0 \end{array}$$

The quantity a is the non-dimensional elastic axis location along the chord of the airfoil measured from the midchord of the airfoil when it is in the neutral position. Since it is non-dimensionalized by the semi-chord of the airfoil, the elastic axis is located half a chord length ahead of the leading edge of the airfoil in this particular case. The airfoil under consideration is the NACA-64A010 (Ames) airfoil operating with a mean angle-of-attack α_0 of 0^o and an amplitude of forced pitching α_{max} of 1^o. A computational mesh composed of 9455 triangular elements is used, as shown in Figure(3).

A damped, neutral, and excited case are run and compared to the corresponding time-implicit solutions in Figures (4)-(6). It should be noted that the BDF2 solutions were rerun using the actual flutter frequency for the first three prescribed periods to facilitate direct comparison of the data. Also, the BDF2 results use 96, 128, and 128 time steps per period for the damped, neutral, and excited cases, respectively. As can be seen from these figures, there is close agreement between the time-implicit and time-spectral solutions, indicating that the BDFTS method is capable of solving the coupled fluid/structure equations. Most importantly, the solutions exhibit the correct flutter response, i.e. damped, neutral, or excited. The cases presented in Figures (4)-(6) were all run at a free stream Mach number $M_\infty = 0.75$, using fifteen time instances for the damped and excited cases and seven time instances for the neutral case, and at the flutter velocity indicated by the corresponding figure caption. In previous work (Ref. 20), it was noted that, although BDFTS and BDF2 response plots match almost exactly for the neutral response, the BDFTS response decayed more slowly in the damped case and grew more slowly in the excited case. This discrepancy is not observed in the current work and was resolved by im-

plicitly coupling the fluid and structure equations (coupling was explicit in previous work) and using more time instances (previous work used a mere five time instances per period).

Also noted in previous work (Ref. 20) was the requirement that $V_f < 0.7$ to produce convergence. It was hypothesized that stronger coupling was needed to converge cases where the structure previously lacked sufficient stiffness to allow for convergence. This hypothesis proved to be correct as the implicit coupling now present in the BDFTS aeroelastic method allows for the solution of all the same flutter problems that were attempted and converged using the time-implicit method.

Rotary Wing Aeroelastic Response

To validate the capabilities of our time-spectral aeroelastic method to accommodate rotorcraft aeroelasticity problems, we devise a two-dimensional test problem. This simulation is analogous to taking a single section of a rotor blade, for example at 60-70% span, and simulating the flow around it independently of the other sections of the rotor. As such, a NACA-0012 airfoil is prescribed a cyclic input:

$$\theta_{con} = \theta_p + \theta_{cyc} \sin(\omega_\theta t) \tag{53}$$

the airfoil is then allowed to respond aeroelastically, both in pitch and plunge, to the aerodynamic forces on it. This can be though of as a flapping blade (plunge response) with a pitch link of finite stiffness (aeroelastic pitch response). Despite the different airfoil being used, the structural parameters are the same as in the fixed wing case, above, with the exception that the value $\mu = 64$ in this case. The computational mesh is composed of 8747 triangular elements, as shown in Figure (7). These structural parameters and this mesh are used for the remaining computations.

Figures (8) and (9) plot both the control input and the the aeroelastic response, pitch and plunge, of the airfoil to the control input: $\theta_p = 0^o$, $\theta_{cyc} = 1^o$, and $k_\theta = 0.05$, where k_θ is the reduced frequency of the control input, which is related to the angular frequency of control input by equation (28). For a rotor blade with an aspect ratio of 15, these control inputs would correspond to the airfoil section at 67% span. These cases and all remaining cases are run at a freestream Mach number $M_\infty = 0.75$ for consistency. Both Figures (8) and (9) show good agreement between the time-implicit (using 64 time steps per period) and time-spectral results (using 5 and 15 time instances, respectively) and were run at the flutter velocity V_f as indicated in the figure, with higher flutter velocity corresponding to lower structural stiffness.

Gust Response

Gust responses for periodic gusts are presented in the following subsections. Two different gust profiles are used. Profile *A* is a short gust such that each gust is only 10% of the length between gust peaks. Profile *B* is a long gust whose length is fully half the length between gust peaks. Both gusts have a non-dimensional peak velocity $v_{g,max} = 0.0155$ which corresponds to an effective 1^o increase in the airfoil angle of attack. Both gust profiles repeat with a reduced frequency of $k_g = 0.05$ and have their leading edges initially positioned a full half period in front of the airfoil's leading edge (31.4159 chords). Figure (10) presents a graphical representation of the two gust profiles just described. The two black bars represent the period of the gusts (peak to peak distance), while the collection of blue dots shows the location and chord of the airfoil in relation to the initial position of the gusts.

The following subsections compare time-spectral to time-implicit results for these two gust profiles, first for a fixed wing and then for a simulated rotary-wing section with cyclic control input.

Fixed Wing Gust Response: In the pursuit of the aeroelastic solution of fixed wing response to the two gust profiles, we first hold the airfoil rigid at zero angle of attack and plot the forces resulting from the gust passing by the rigid airfoil. Figures (11) and (12) plot the lift and moment generated by gust profiles A and B, respectively. Figure (11) uses 55 time instances in order to achieve good agreement between time-spectral and time-implicit results, while only 15 time instances are required to produce good agreement for the longer gust B. For both gust profiles, 128 time steps per period are used for the time-implicit results.

Having obtained good agreement for the forces generated on the rigid airfoil, the same gust profiles are applied to the aeroelastic system. For both profiles, and, in fact, all results presented subsequently in this paper, the flutter velocity is held constant at $V_f = 0.25$ which corresponds to a structural reduced frequency of $k_c = 0.50$ or $10x$ the reduced frequency of the gusts. Figures (13) and (14) plot the modified lift and moment experienced by the airfoil as it is allowed to respond aeroelastically. As can be seen, good agreement is obtained for the forces for both gust profiles. Likewise, Figures (15) and (16) relate the aeroelastic response the the two gust profiles. Again, good agreement is obtained between the time-implicit and time-spectral results. The preceding solutions use 1024 time steps and 45 time instances per period for gust A and 512 time steps and 27 time instances per period for gust B.

Rotary Wing Gust Response: The rotary wing gust response involves the NACA-0012 airfoil with the same prescribed control input as used in the "Rotary Wing Aeroelastic Response" subsection, above. It should be emphasized that the frequency of control input and the gust frequency are identical, indicating that the gust interacts with the blade once per revolution. First, the control input is coupled with a rigid airfoil and the resultant forces and moments are obtained. Figures (17) and (18) show the lift and pitching moment coefficients for gusts A and B, respectively. As can be seen, good agreement is obtained between the time-spectral and time-implicit results by using 55 time instances and 96 time steps per period for gust profile A and 15 time instances and 128 time steps per period for gust profile B.

With agreement of the force and moments obtained, we now remove the rigidity constraint and allow the airfoil to respond aeroelastically. As noted previously, a flutter velocity of $V_f = 0.25$ is used. Figures (19) and (20) plot the lift force and pitching moment produced by the aeroelastically pitching airfoil. Similarly, Figures (21) and (22) plot the aeroelastic response of the same airfoil to the two gust profiles. Once again, good agreement between time-spectral and time-implicit results is obtained with the use of a sufficient number of time instances, as noted in the legends of these figures. Also note that the time-implicit results in both figures use 256 time steps per period.

Time-solution Accuracy Convergence Study: The above results have established that, given sufficient temporal resolution, the time-spectral and time-implicit schemes converge to essentially identical results. While the BDF2 time-implicit scheme is nominally second-order accurate, theoretically the time-spectral method should converge exponentially in time (faster than any polynomial order) as the number of time instances is increased. In order to study the temporal error convergence of both schemes, the test case consisting of the airfoil aeroelastic response to gust profile A is revisited. BDF2 solutions for this test case using 224, 256, 512 and 1024 time steps per period are computed and the moment coefficient and pitch response are shown in Figures (23) and (24), respectively. As the number of time steps is increased, the discrepancies between the consecutive solutions is seen to diminish. This exercise is repeated in Figures (25) and (26) for the time-spectral method, using 21, 33, 45, 55, and 79 time instances, where the solution is also seen to converge as the number of time instances is increased.

In order to evaluate the temporal error in these various solutions, an "exact" reference solution is obtained using 5096 BDF2 time steps per period. The error in the various BDF2 and time-spectral solutions is then estimated by computing the difference between the time histories generated by these different solutions and that of the reference solution. Figure (27) depicts the computed temporal error for these solutions. The BDF2 error plot has a slope of 2.05, which is slightly higher than the expected design accuracy of 2.00. The time-spectral error decreases faster, with a maximum slope of 8.84, although exponential convergence is not observed. This may be partly due to the fact that all time instance residuals were "only" converged to 1×10^{-11}, as well as due to the accuracy of the reference solution itself in representing the fully converged temporal problem. We note that for this problem, in order to obtain good agreement between the BDF2 and time-spectral methods, both a very small BDF2 time step (1024 per period) and a high number of time-instances (45) were required. In this case, the total wall-clock time required for both methods was similar.

Conclusions and Future Work

The TS and BDFTS methods have been demonstrated to be capable of solving the coupled unsteady fluid-structure equations and the results have been shown to compare favorably to traditional time-implicit methods. While it is our hope that ultimately time-spectral based methods can be used to solve time-accurate problems with strong periodic content more efficiently than the current state-of-the-art time-implicit methods, this is not always the case at present. In general, as currently implemented, time-spectral based methods are more efficient when any of the following occur:

a) All content can be resolved using at most two harmonics (5 time instances)

b) The time-implicit method requires a large number of periods to finally settle to the time-periodic solution (this is true for a fair number of rotary wing aeroelastic response cases)

c) The time-implicit solution requires a very small time step (as in the fixed-wing gust response to gust profile A)

d) The period of motion is very long

It is expected that a more efficient linear solver, most notably FGMRES with a better preconditioner, such as linear multigrid, will enable time-spectral methods to be more efficient than the time-implicit method in almost all cases.

The present study was primarily aimed to validate the accuracy of time-spectral methods as applied to the problems presented herein. As such, the non-linear residual was required to be less than 1×10^{-11} for each time step of the time-implicit solution to be considered converged and for the overall time-spectral system to be considered converged. This convergence tolerance would be considered to be overly tight by industry standards. Despite the focus on accuracy of the present study, some notable examples of the benefits of the time-spectral method over the time-implicit method merit mention. The first of the two rotary-wing-like simulations presented above ($V_f = 0.50$) had advantages a) and b) listed above and took about $1/2$ the time for the time-spectral solution to complete when compared with the time-implicit solution, on identical hardware. As noted previously, the very small time-step that was needed for a fully-converged, time-implicit solution of the fixed-wing gust response to gust profile A created a scenario where the time-spectral solution took about the same amount of time. A better FGMRES preconditioner for time-spectral methods should make these methods competitive, if not more efficient, in all cases. Additionally, time-spectral methods offer the added benefit that different time instances can be run in parallel, thus allowing more efficient allocation of high-performance computing clusters. As clusters continue to grow larger, a greater ability to adapt to the parallel-computing power available is paramount. Time-spectral methods represent one such adaptation. Even if a time-spectral solution cannot be found more efficiently using the same architecture as a time-implicit solution, it can still be found in less wall-clock time by taking advantage of the additional avenue of parallelism that time-spectral methods provide. Indeed, many time-spectral solutions presented in the current work completed in about the same wall-clock

time or less than the corresponding time-implicit solution, even though resources were not always available to utilize the maximum possible amount of parallelism.

In addition to solver improvements, other improvements also must be made in order for time-spectral methods to become mainstream for aeroelastic problems. First, a method must be found to allow for the resolution of the flutter period as the BDFTS, fixed-wing aeroelastic solution progresses, instead of being prescribed, as was done herein. Next, as can be seen, the number of time instances needed to completely resolve the harmonic content of a problem varies widely; therefore, a method must be developed by which all problems can be initiated with a few time instances and then time instances can be automatically added as the solution evolves. Basically, a quantification of the uncertainty in a solution can be found and used to perform that is essentitally a time-solution accuracy convergence study as part of the solution procedure itself. This can be thought of as time-instance adaptation, which is analogous to grid adaptation currently used to reduce spatial error. It is expected that the use of sensitivities found by means of the discrete adjoint can be used for time-instance adaptation.

In the near future, the Split Velocity Method will be extended to include the prescription of vortices, and additional cases will be completed in order to simulate blade-vortex interaction (BVI) experienced by rotorcraft. Additionally, gusts that span several blade periods, or are not themselves periodic will be simulated using the BDFTS method.

References

[1]Hall, K. C., Thomas, J. P., and Clark, W. S., "Computation of Unsteady Nonlinear Flows in Cascades Using a Harmonic Balance Technique," *AIAA Journal*, Vol. 40, (5), 2002, pp. 879–886.

[2]McMullen, M., Jameson, A., and Alonso, J. J., "Acceleration of Convergence to a Periodic Steady State in Turbomachineary Flows," AIAA Paper 2001-0152, Jan. 2001.

[3]McMullen, M., Jameson, A., and Alonso, J. J., "Application of a Non-Linear Frequency Domain Solver to the Euler and Navier-Stokes Equations," AIAA Paper 2002-0120, Jan. 2002.

[4]Gopinath, A. K. and Jameson, A., "Time Spectral Method for Periodic Unsteady Computations over Two- and Three-Dimensional Bodies," AIAA Paper 2005-1220, Jan. 2005.

[5]van der Weide, E., Gopinath, A. K., and Jameson, A., "Turbomachineary Applications with the Time Spectral Method," AIAA Paper 2005-4905, June 2005.

[6]Lee, K.-H., Alonso, J. J., and van der Weide, E., "Mesh Adaptation Criteria for Unsteady Periodic Flows Using a Discrete Adjoint Time-Spectral Formulation," AIAA paper 2006-0692, Jan. 2006.

[7]Sankaran, S., Gopinath, A., Weide, E. V. D., Tomlin, C., and Jameson, A., "Aerodynamics and Flight Control of Flapping Wing Flight Vehicles: A Preliminary Computational Study," AIAA 2005-0841, Jan. 2005.

[8]Choi, S., Potsdam, M., Lee, K., Iaccarino, G., and Alonso, J. J., "Helicopter Rotor Design Using a Time-Spectral and Adjoint-Based Method," AIAA 2008-5810, Sep. 2008.

[9]Choi, S. and Datta, A., "CFD Prediction of Rotor Loads using Time-Spectral Method and Exact Fluid-Structure Interface," AIAA 2008-7325, Aug. 2008.

[10]Yang, Z. and Mavriplis, D. J., "Time spectral method for quasi-periodic unsteady computation on unstructured meshes." AIAA Paper 2010-5034, June 2010.

[11]Yang, Z., Mavriplis, D. J., and Sitaraman, J., "Prediction of Helicopter Maneuver Loads Using BDF/Time Spectral Method on Unstructured Meshes," AIAA Paper 2011-1122, June 2011.

[12]Mavriplis, D. J., Yang, Z., and Mundis, N. L., "Extensions of Time Spectral Methods for Practical Rotorcraft Problems," AIAA paper 2012-0423, Jan. 2012.

[13]Alonso, J. J. and Jameson, A., "Fully-Implicit Time-Marching Aeroelastic Solutions," AIAA paper 1994-0056, Jan. 1994.

[14]Mani, K. and Mavriplis, D. J., "Linearization of the Coupled Unstead Fluid-Structure Equations: Application to Flutter Control," AIAA paper 2008-6242, August 2008.

[15]Willcox, K. and Peraire, J., "Aeroelastic computations in the time domain using unstructured meshes," *International Journal for Numerical Methods in Engineering*, Vol. 40-13, 1997.

[16]Leishman, J. G., *Principles of Helicopter Aerodynamics*, Cambridge U. P., 2006.

[17]Canuto, C., Hussaini, M. Y., Quarteroni, A., and Zang, T. A., *Spectral Methods in Fluid Dynamics*, Springer, 1987.

[18]Hesthaven, J., Gottlieb, S., and Gottlieb, D., *Spectral Methods for Time-Dependent Problems*, Cambridge Monographs on Applied and Computational Mathematics, 2007.

[19]Gottlieb, D. and Orszag, S. A., "Numerical Analysis of Spectral Methods: Theory and Applications," CBMS-26, Regional Conference Series in Applied Mathematics, SIAM,Philadelphia, PA, 1977.

[20]Mundis, N. L. and Mavriplis, D. J., "Quasi-Periodic Time Spectral Method for Aeroelastic Flutter Analysis," AIAA paper 2013-0638, Jan. 2013.

[21]Sitaraman, J., *CFD based unsteady aerodynamic modeling for rotor aeroelastic analysis*, Ph.D. thesis, University of Maryland, 2003.

[22]Singh, R. and Baeder, J., "Generalized Moveing Gust Response Using CFD with Application to Airfoil-Vortex Interaction," AIAA paper 1997-2208, 1997.

[23]Zaide, A. and Raveh, D., "Numerical simulation and reduced-order modeling of airfoil gust response," *AIAA Journal*, Vol. 44, 2006, pp. 1826–1834.

[24]D. Jones, C. W. and Gaitonde, A., "Simulation of airfoil gust responses using prescribed velocities," IFASD, 2011.

[25]C. Wales, D. J. and Gaitonde, A., "Reduced order modelling for aeroelastic aerofoil response to a gust," AIAA paper 2013-0790, 2013.

[26]Isogai, K., "Transonic Dip Mechanism of Flutter of a Sweptback Wing: Part II," *AIAA Journal*, Vol. 17, 1981, pp. 1240–1242.

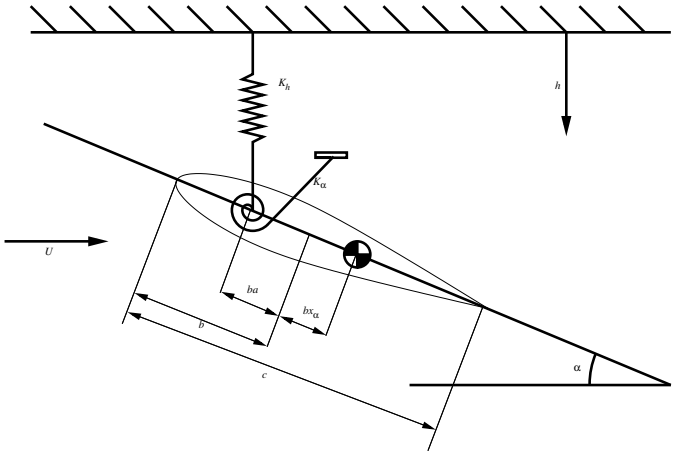

Fig. 1: Two degree of freedom 2-D aeroelastic problem schematic

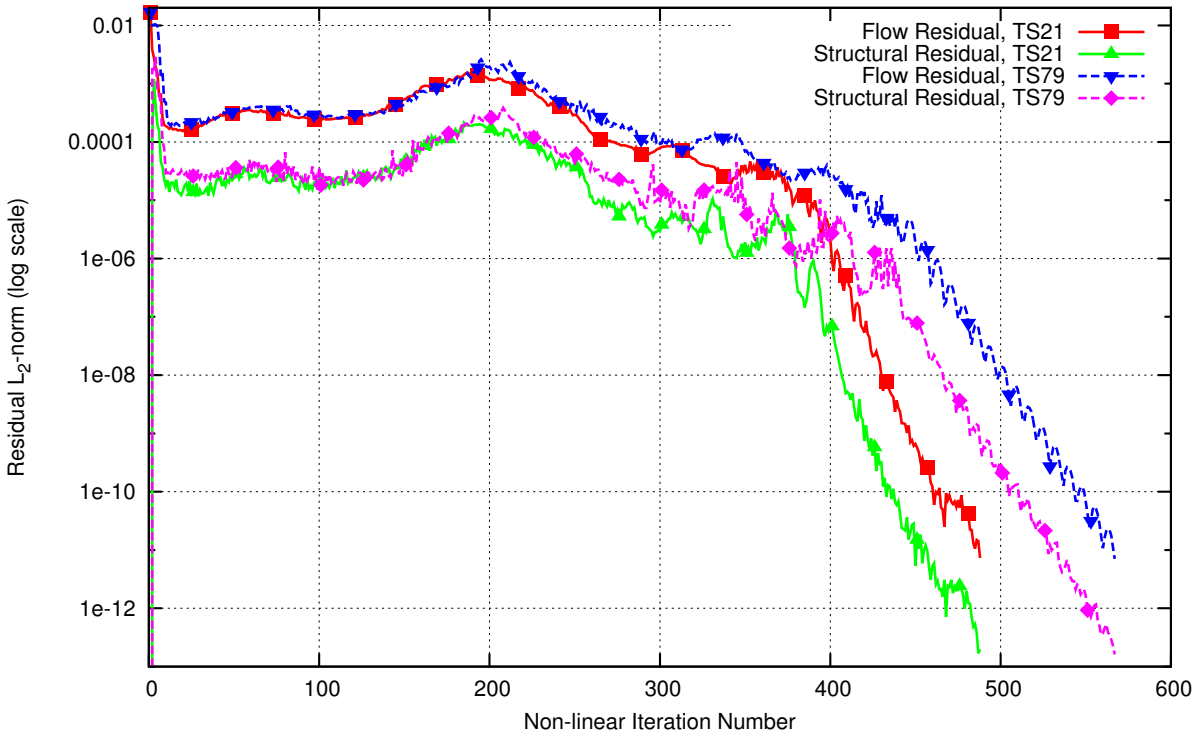

Fig. 2: Convergence of fixed wing gust response for the time-spectral aeroelastic method: Gust Profile A ($M_\infty = 0.75, V_f = 0.25$; 21 and 79 time instances per period)

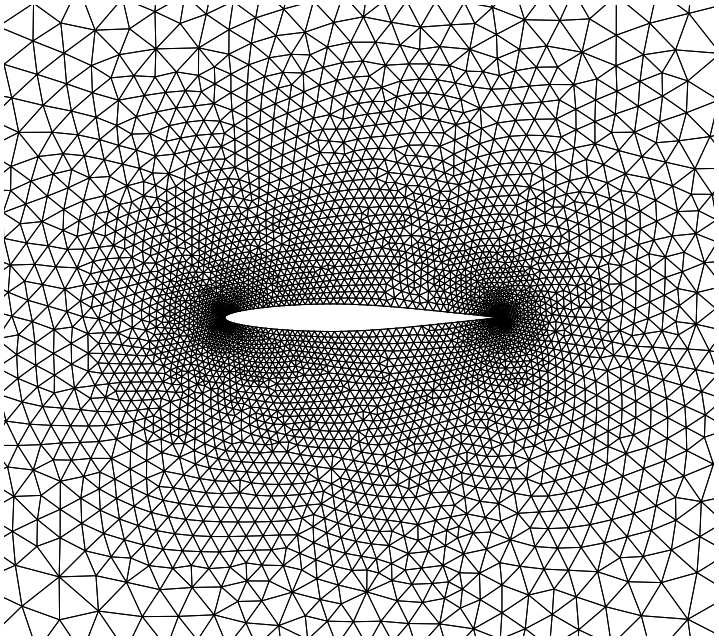

Fig. 3: Near-body computational mesh for the NACA-64a010 airfoil (4821 nodes, 9455 elements)

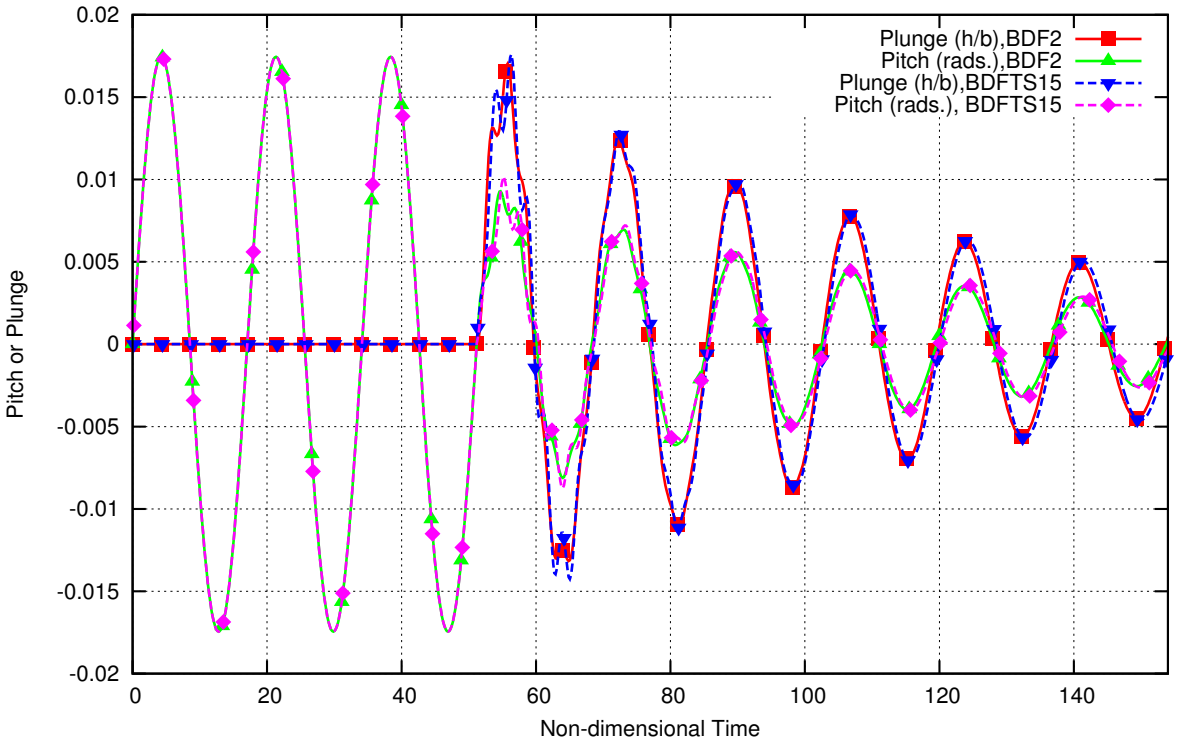

Fig. 4: Comparison of fixed wing aeroelastic response for BDF2 and BDFTS methods: Damped response ($M_\infty = 0.75, V_f = 0.5$; 96 time steps and 15 time instances per period)

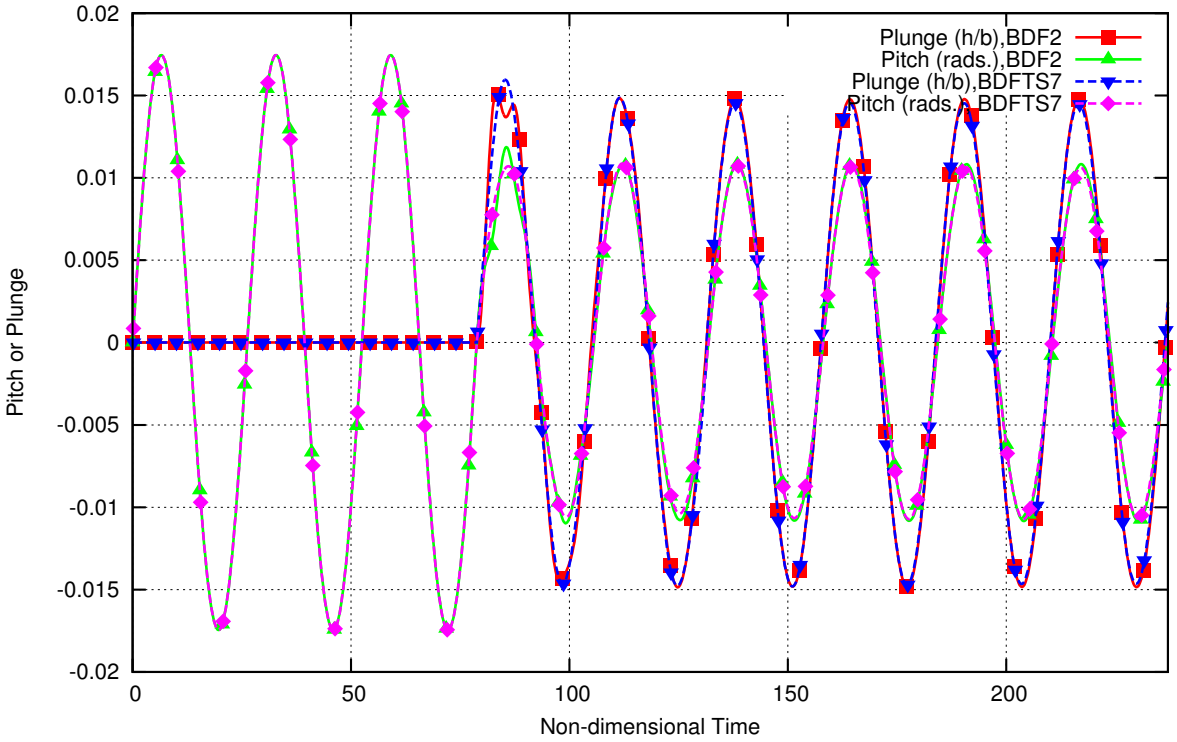

Fig. 5: Comparison of fixed wing aeroelastic response for BDF2 and BDFTS methods: Neutral response ($M_\infty = 0.75, V_f = 1.116$; 128 time steps and 7 time instances per period)

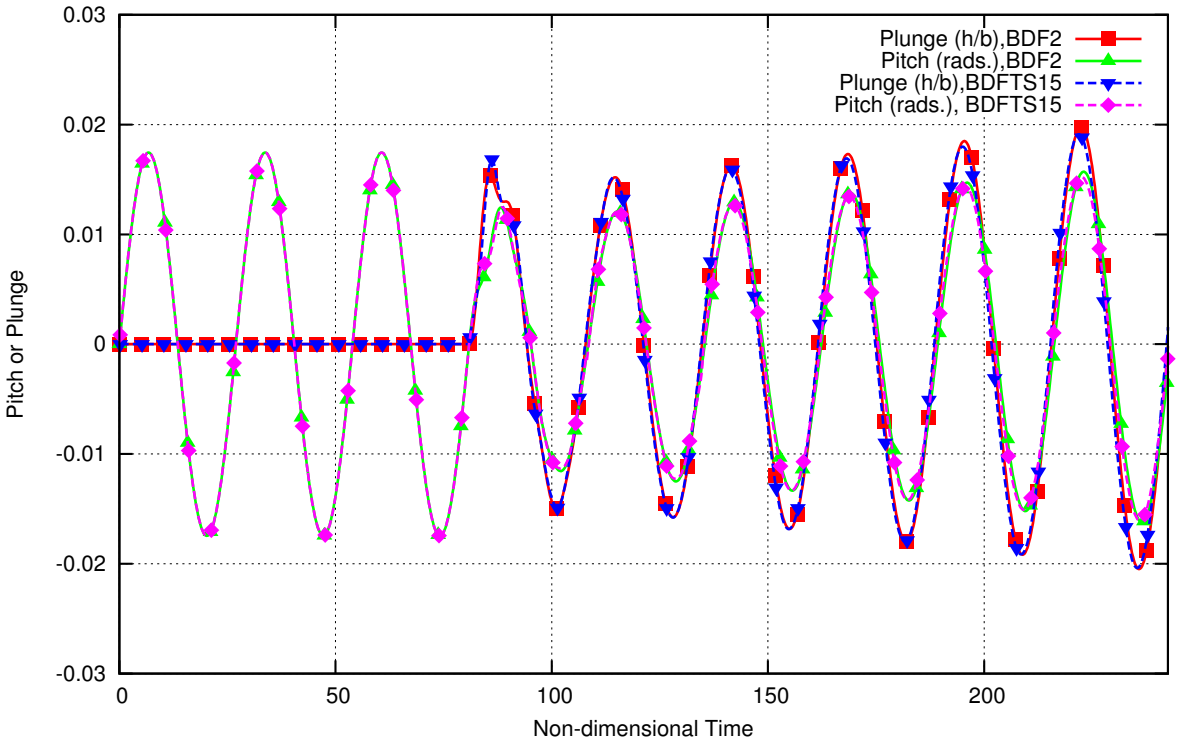

Fig. 6: Comparison of fixed wing aeroelastic response for BDF2 and BDFTS methods: Excited response ($M_\infty = 0.75, V_f = 1.2$; 128 time steps and 15 time instances per period)

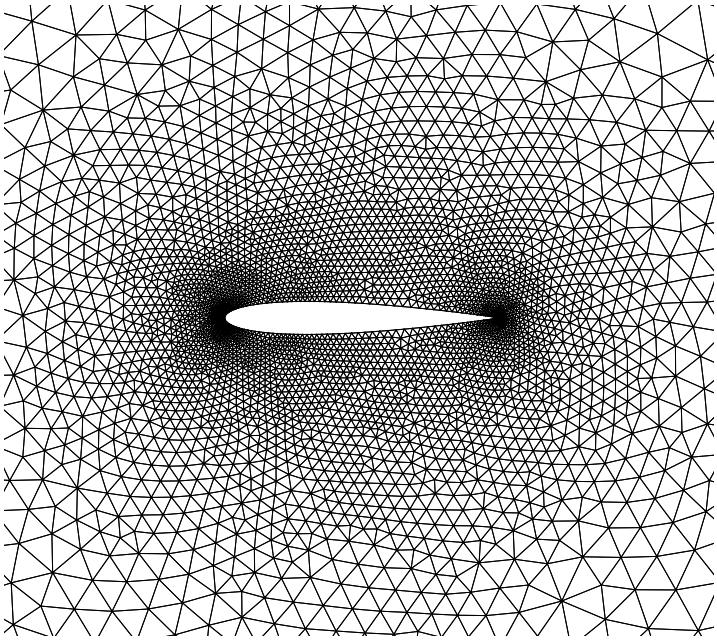

Fig. 7: Near-body computational mesh for the NACA-0012 airfoil (4471 nodes, 8747 elements)

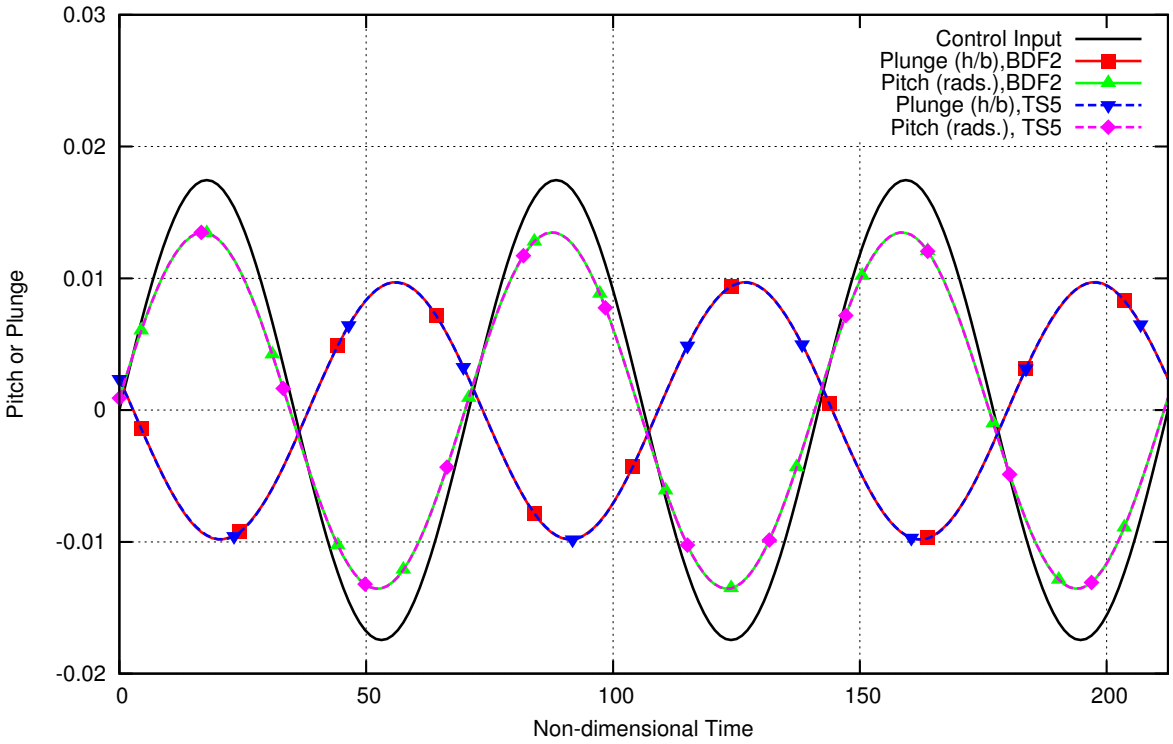

Fig. 8: Comparison of rotary wing aeroelastic response for BDF2 and TS methods
($M_\infty = 0.75, V_f = 0.5$; 64 time steps and 5 time instances per period)

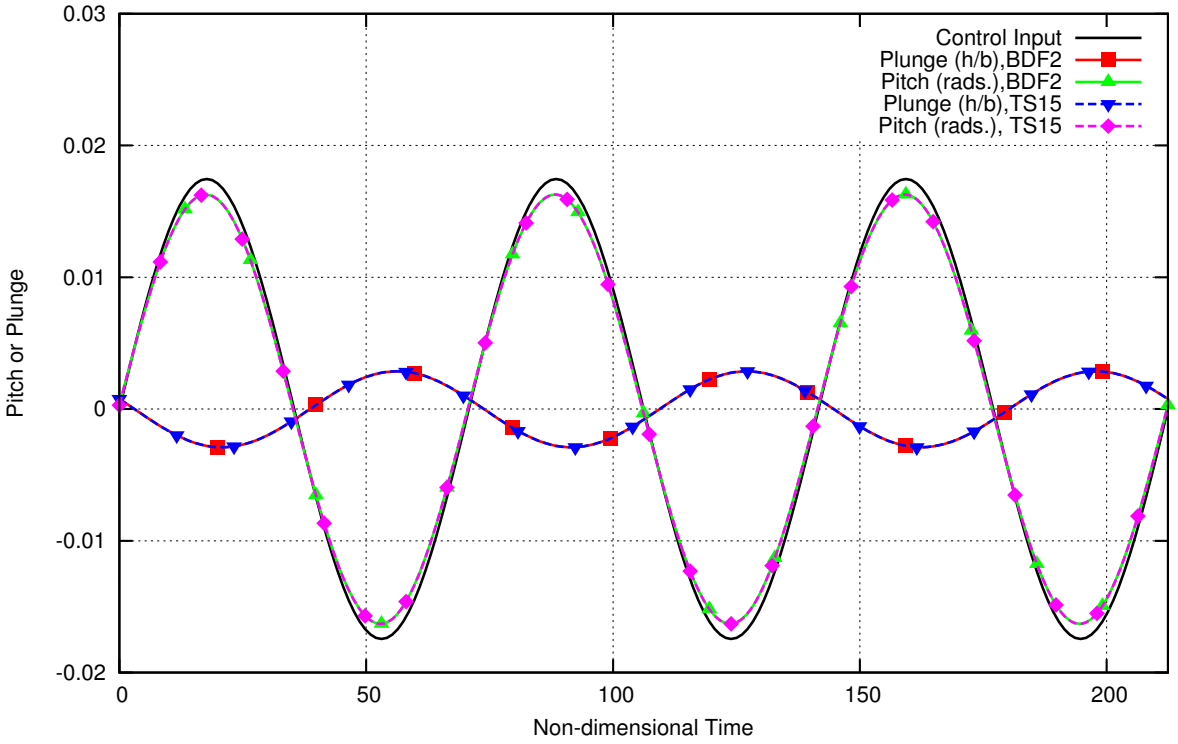

Fig. 9: Comparison of rotary wing aeroelastic response for BDF2 and TS methods
($M_\infty = 0.75, V_f = 0.25$; 64 time steps and 15 time instances per period)

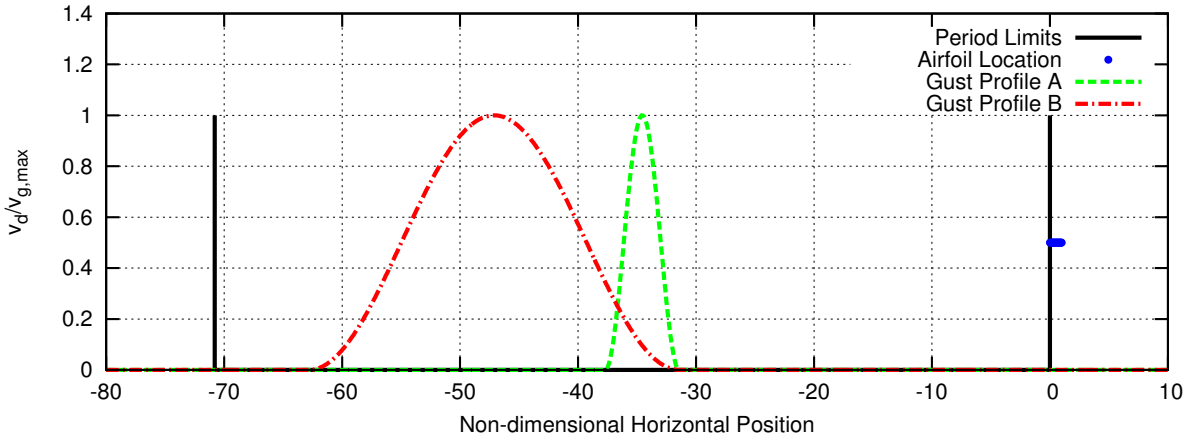

Fig. 10: Periodic Gust Profiles at their initial positions and relative size of airfoil $@x = 0$

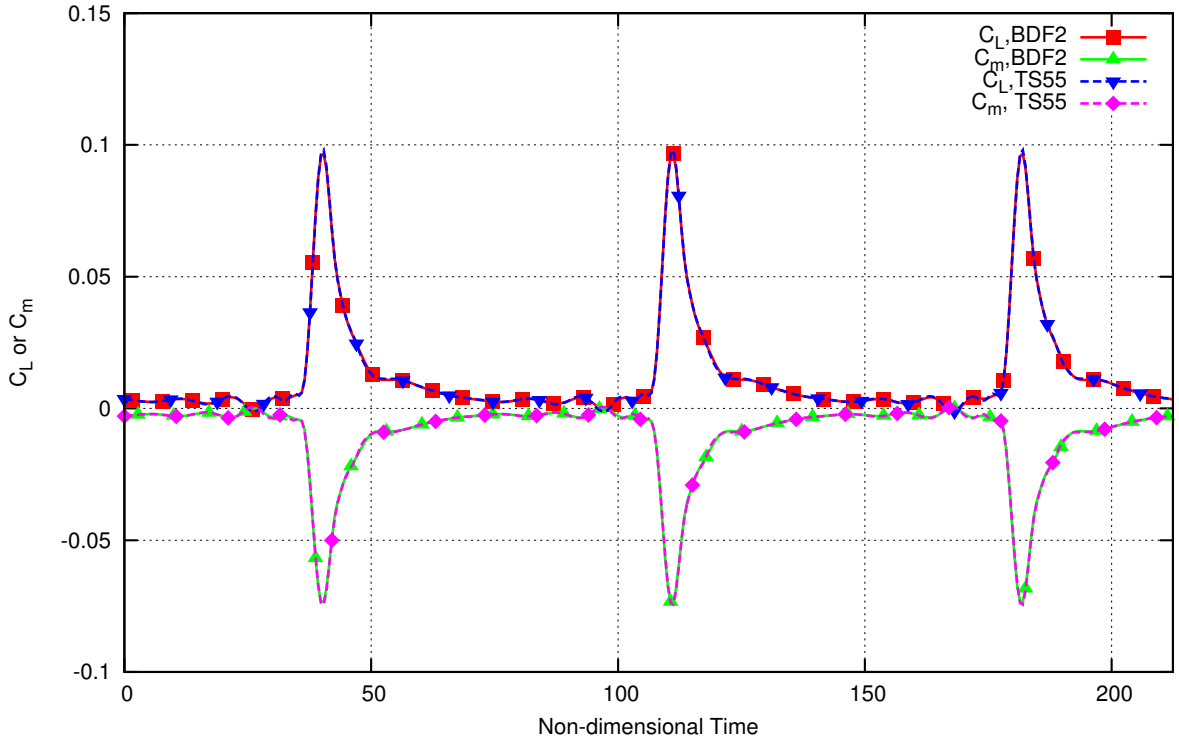

Fig. 11: Comparison of static, fixed wing gust forces, gust profile A (short gust), for BDF2 and TS methods ($M_\infty = 0.75$; 128 time steps and 55 time instances per period)

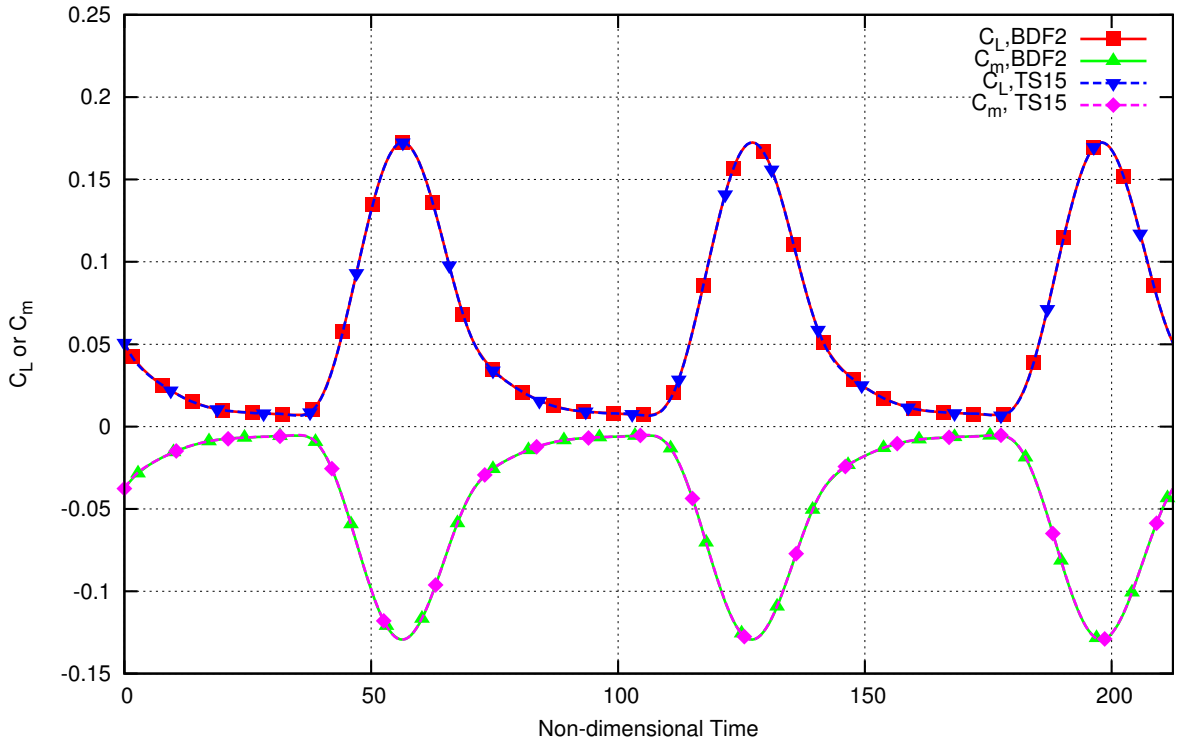

Fig. 12: Comparison of static, fixed wing gust forces, gust profile B (long gust), for BDF2 and TS methods ($M_\infty = 0.75$; 128 time steps and 15 time instances per period)

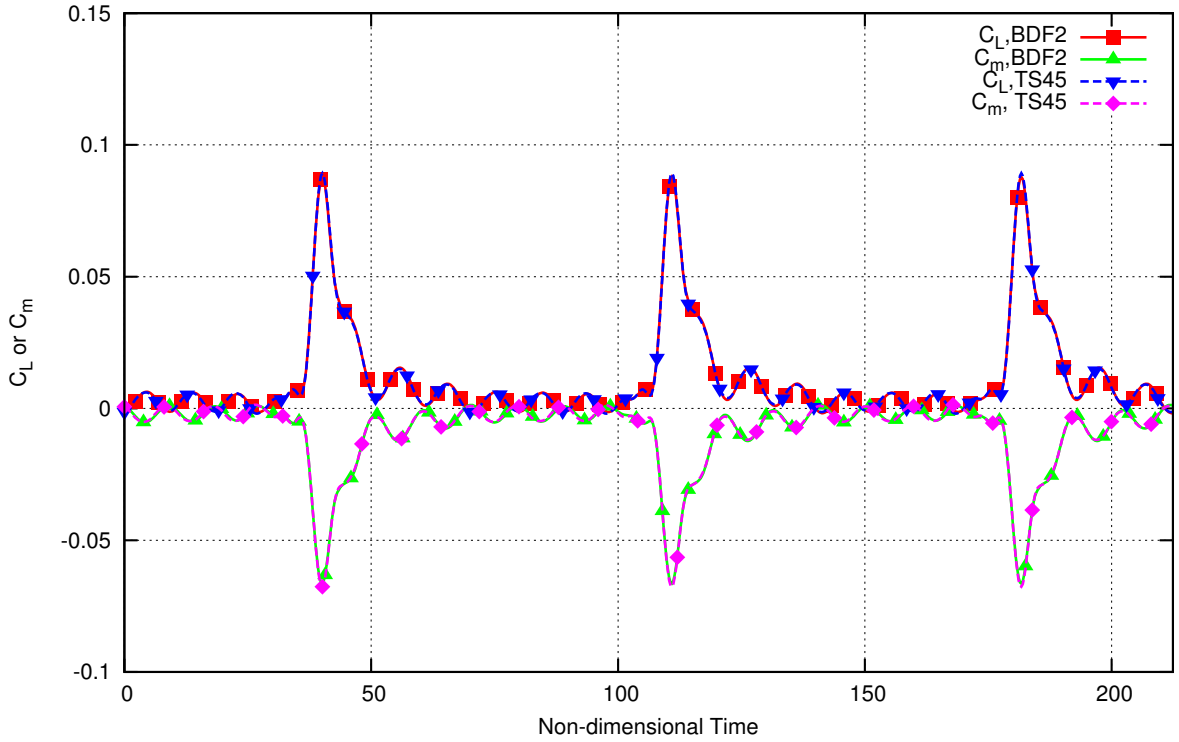

Fig. 13: Comparison of aeroelastic, fixed wing gust forces, gust profile A (short gust), for BDF2 and TS methods ($M_\infty = 0.75, V_f = 0.25$; 256 time steps and 45 time instances per period)

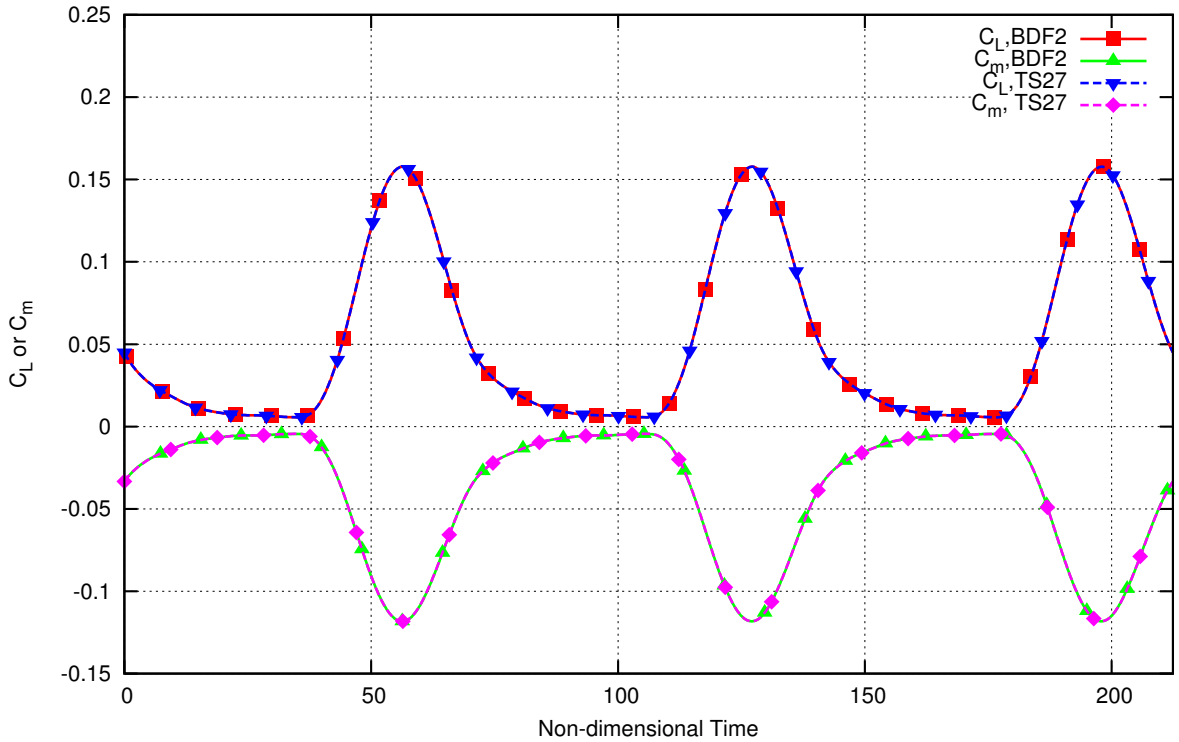

Fig. 14: Comparison of aeroelastic, fixed wing gust forces, gust profile B (long gust), for BDF2 and TS methods ($M_\infty = 0.75, V_f = 0.25$; 512 time steps and 27 time instances per period)

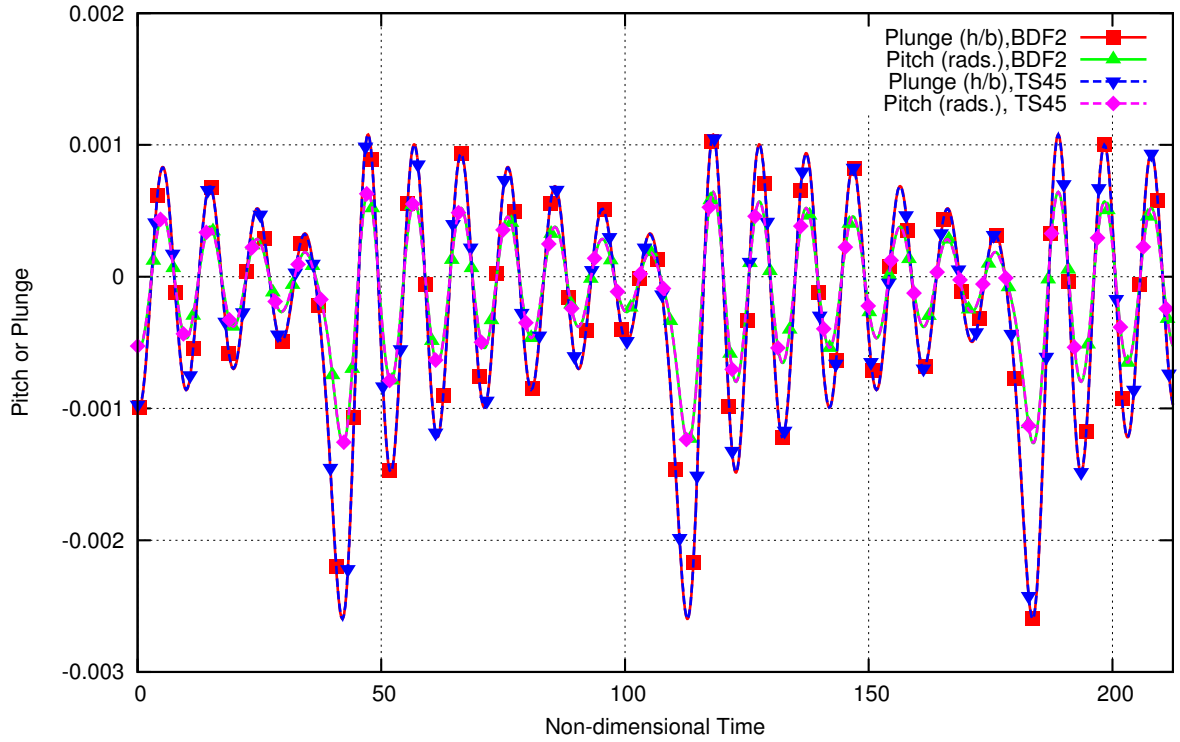

Fig. 15: Comparison of aeroelastic, fixed wing gust response, gust profile A (short gust), for BDF2 and TS methods ($M_\infty = 0.75, V_f = 0.25$; 1024 time steps and 45 time instances per period)

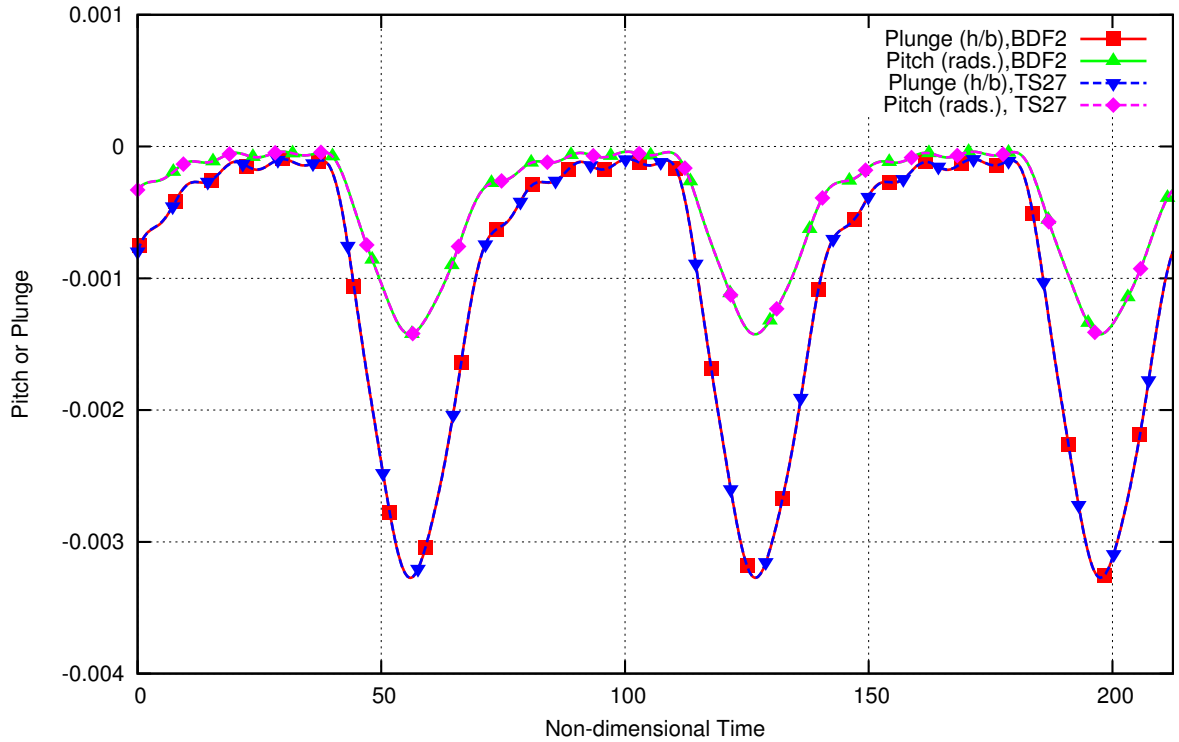

Fig. 16: Comparison of aeroelastic, fixed wing gust response, gust profile B (long gust), for BDF2 and TS methods ($M_\infty = 0.75, V_f = 0.25$; 512 time steps and 27 time instances per period)

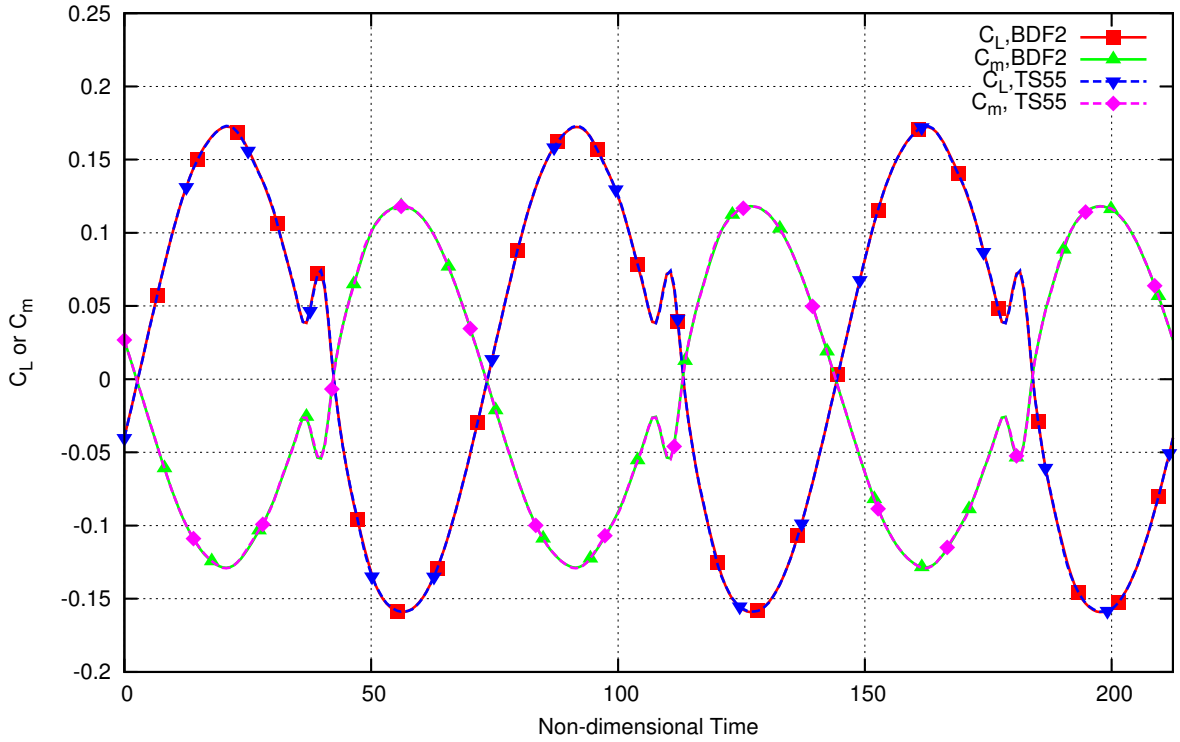

Fig. 17: Comparison of static, rotary wing gust forces, gust profile A (short gust), for BDF2 and TS methods ($M_\infty = 0.75$; 96 time steps and 55 time instances per period)

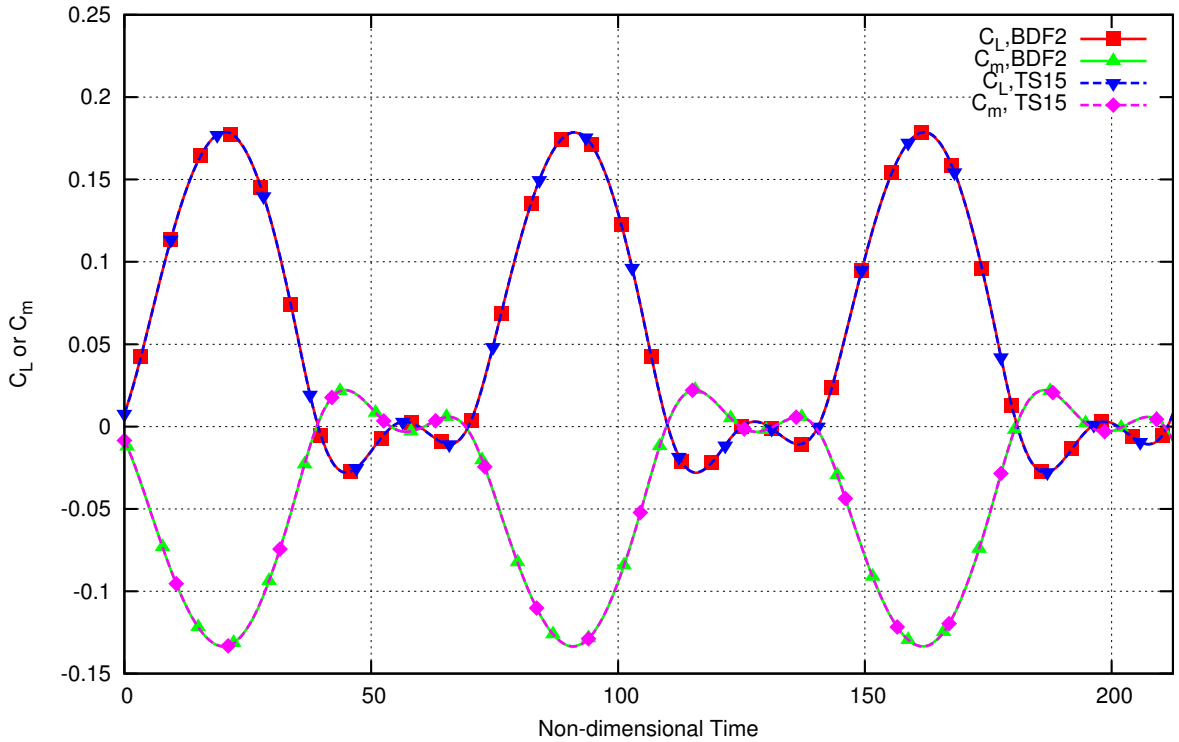

Fig. 18: Comparison of static, rotary wing gust forces, gust profile B (long gust), for BDF2 and TS methods ($M_\infty = 0.75$, 128 time steps and 15 time instances per period)

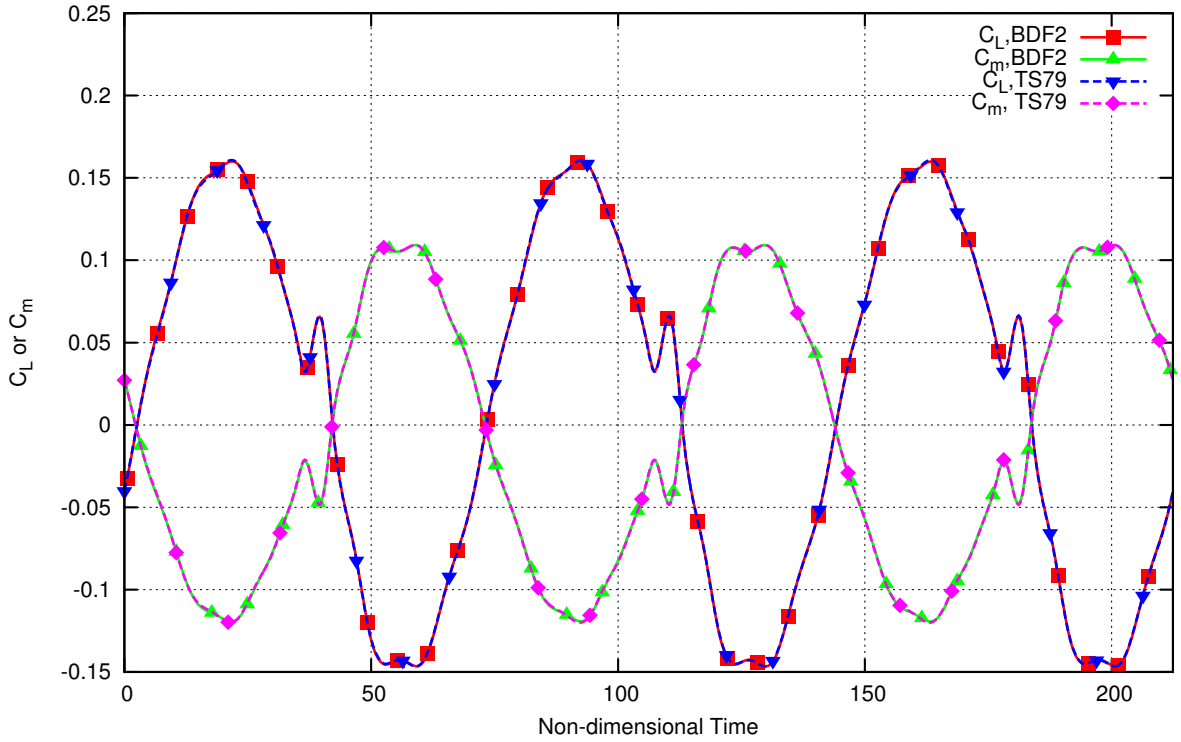

Fig. 19: Comparison of aeroelastic, rotary wing gust forces, gust profile A (short gust), for BDF2 and TS methods ($M_\infty = 0.75, V_f = 0.25$; 256 time steps and 79 time instances per period)

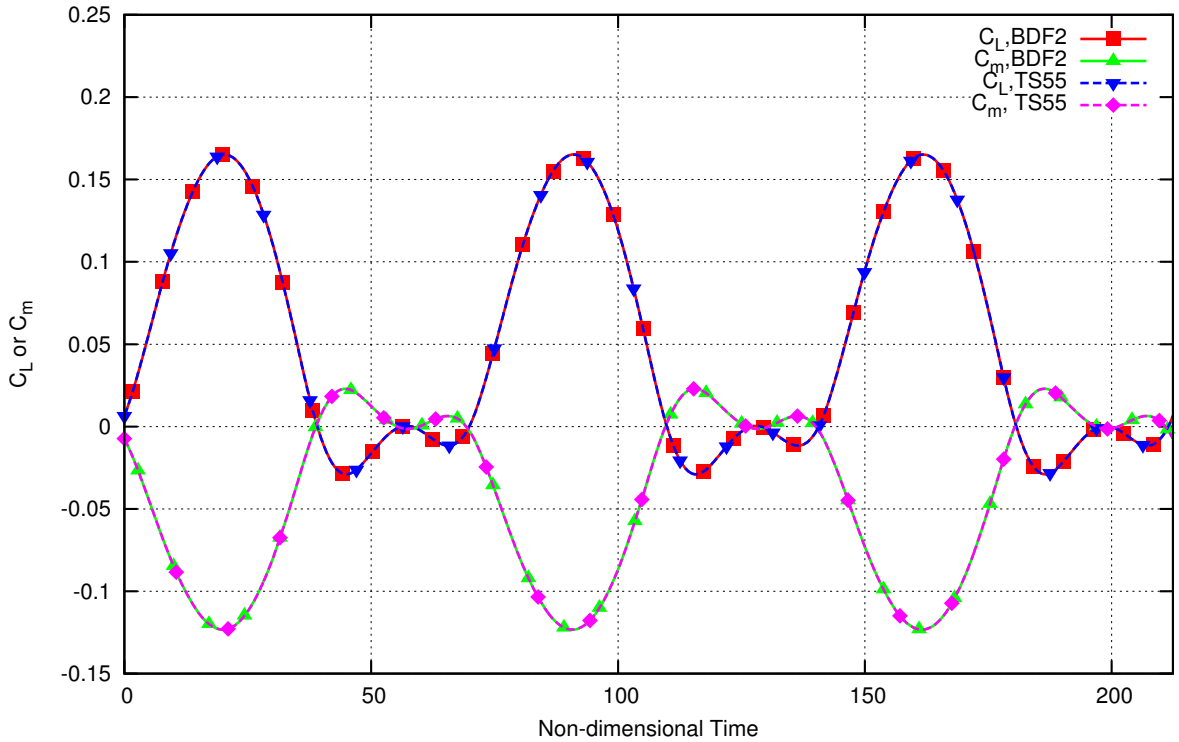

Fig. 20: Comparison of aeroelastic, rotary wing gust forces, gust profile B (long gust), for BDF2 and TS methods ($M_\infty = 0.75, V_f = 0.25$; 256 time steps and 55 time instances per period)

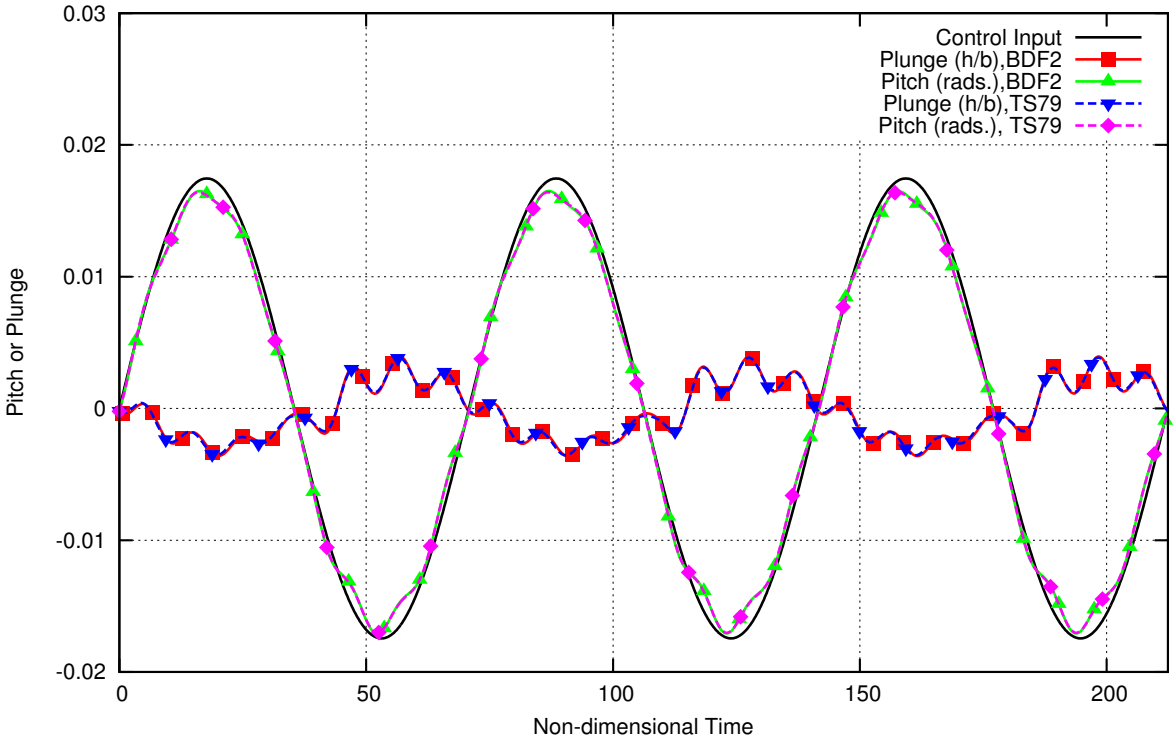

Fig. 21: Comparison of aeroelastic, rotary wing gust response, gust profile A (short gust), for BDF2 and TS methods ($M_\infty = 0.75, V_f = 0.25$; 256 time steps and 79 time instances per period)

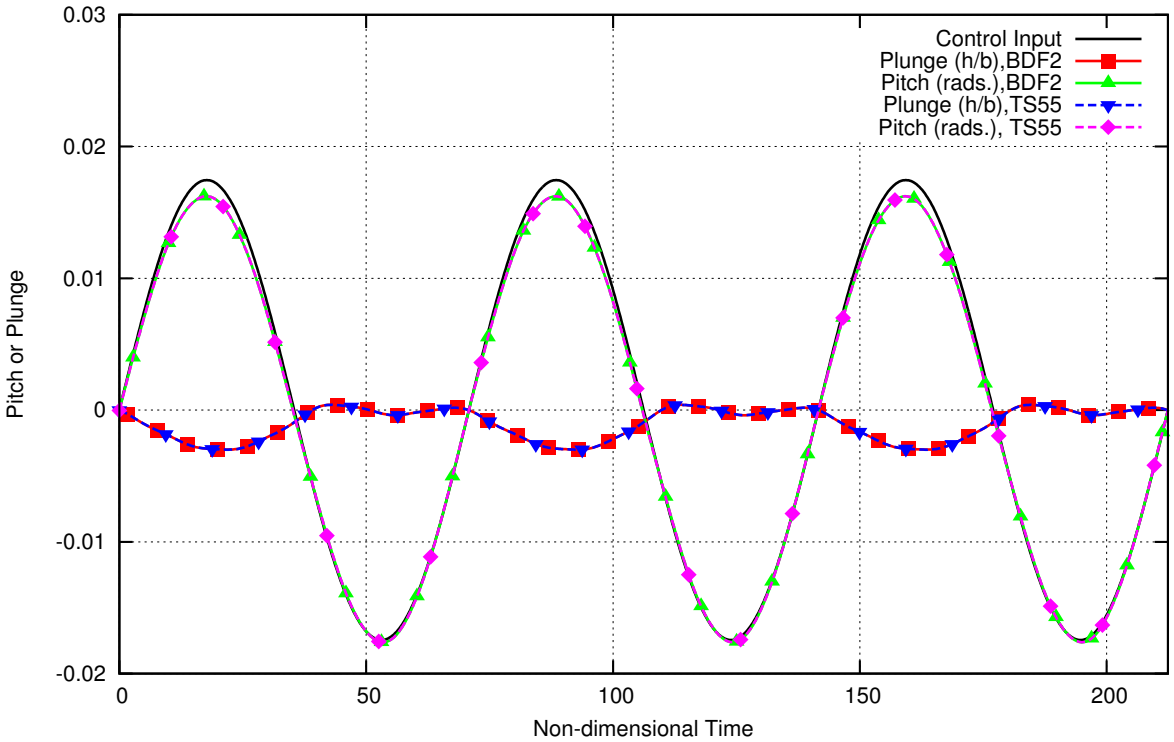

Fig. 22: Comparison of aeroelastic, rotary wing gust response, gust profile B (long gust), for BDF2 and TS methods ($M_\infty = 0.75, V_f = 0.25$; 256 time steps and 55 time instances per period)

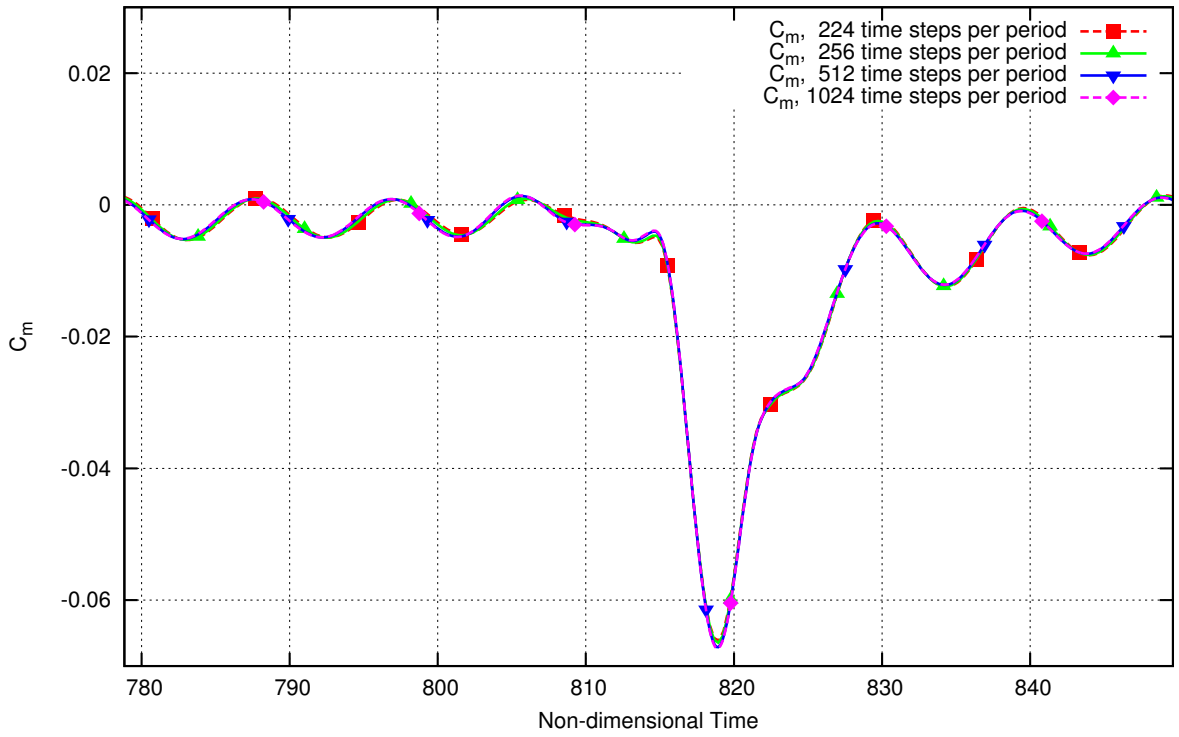

Fig. 23: Comparison of aeroelastic, fixed wing gust moment, gust profile A (short gust), for BDF2 method with varying numbers of time steps
($M_\infty = 0.75, V_f = 0.25$; 160, 256, 512, and 1024 time steps per period)

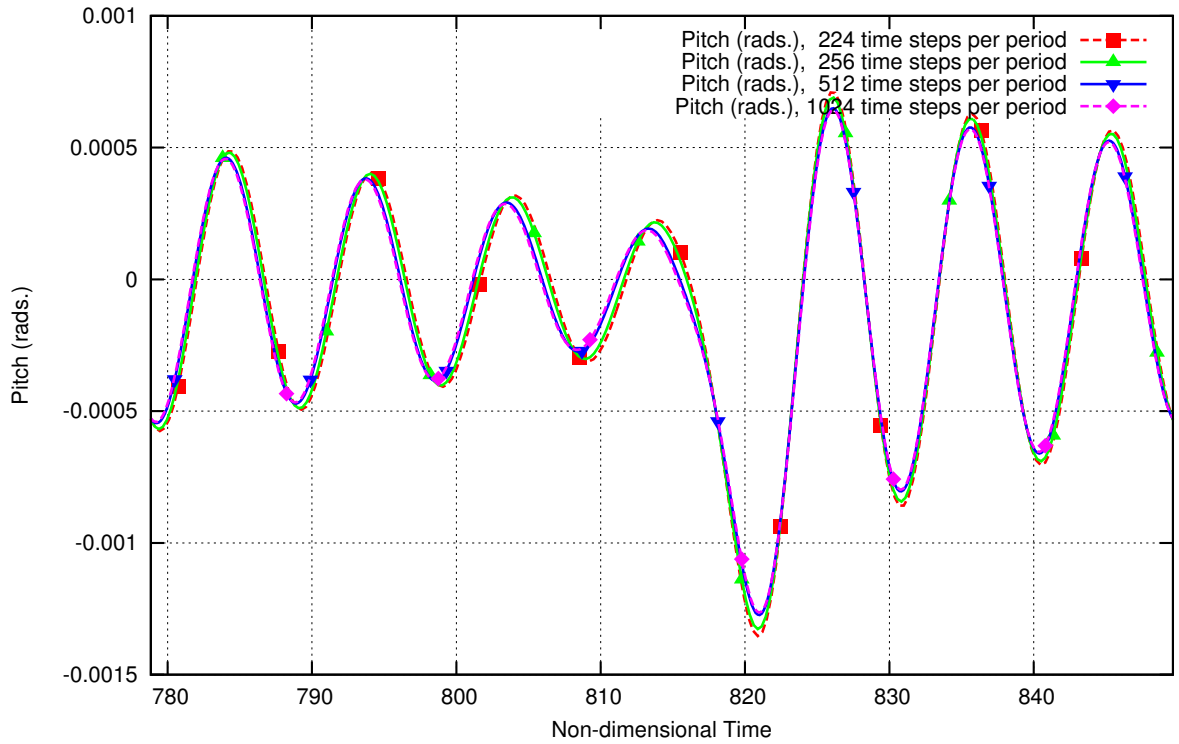

Fig. 24: Comparison of aeroelastic, fixed wing gust pitch, gust profile A (short gust), for BDF2 method with varying numbers of time steps
($M_\infty = 0.75, V_f = 0.25$; 160, 256, 512, and 1024 time steps per period))

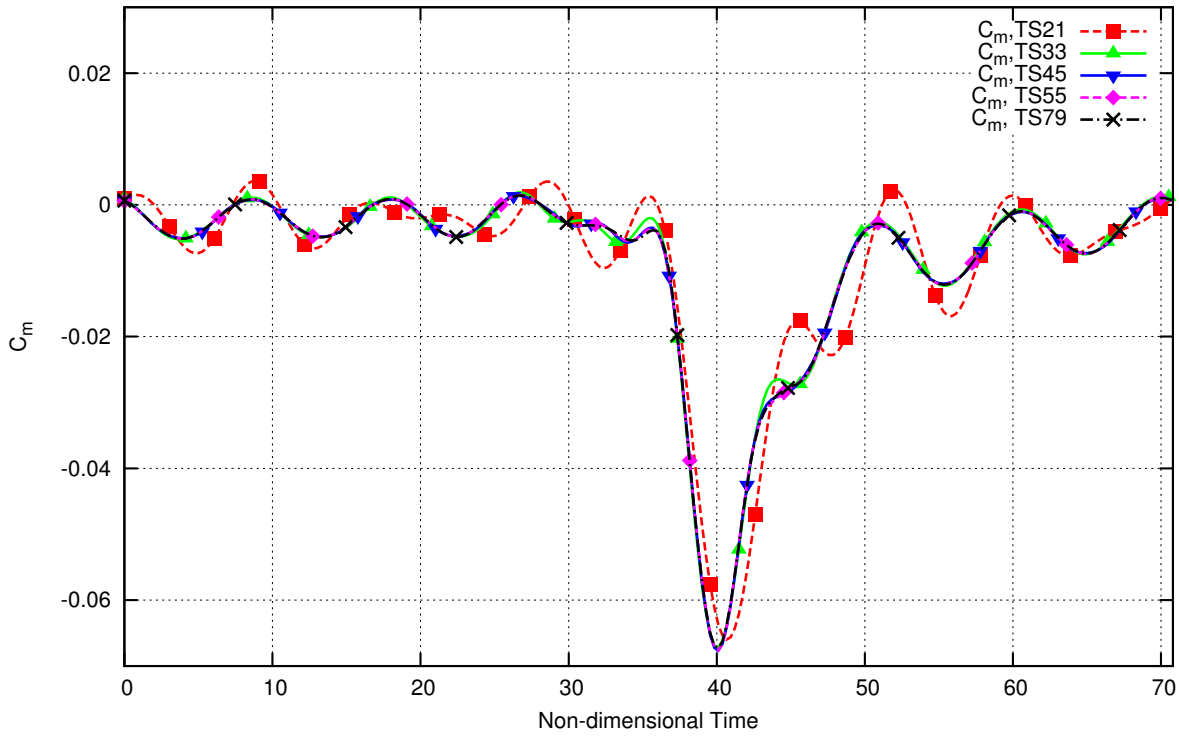

Fig. 25: Comparison of aeroelastic, fixed wing gust moment, gust profile A (short gust), for TS method with varying numbers of time instances
($M_\infty = 0.75, V_f = 0.25$; 21, 33, 45, 55, and 79 time instances per perriod)

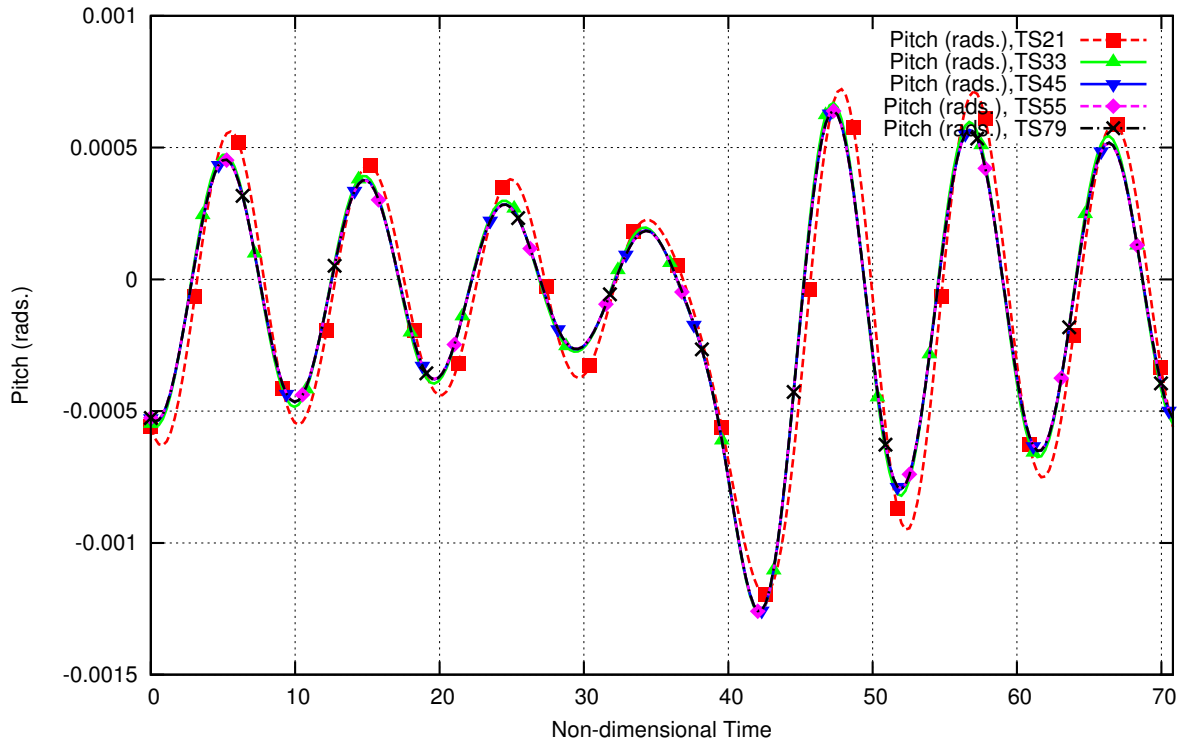

Fig. 26: Comparison of aeroelastic, fixed wing gust pitch, gust profile A (short gust), for TS method with varying numbers of time instances
($M_\infty = 0.75, V_f = 0.25$; 21, 33, 45, 55, and 79 time instances per period)

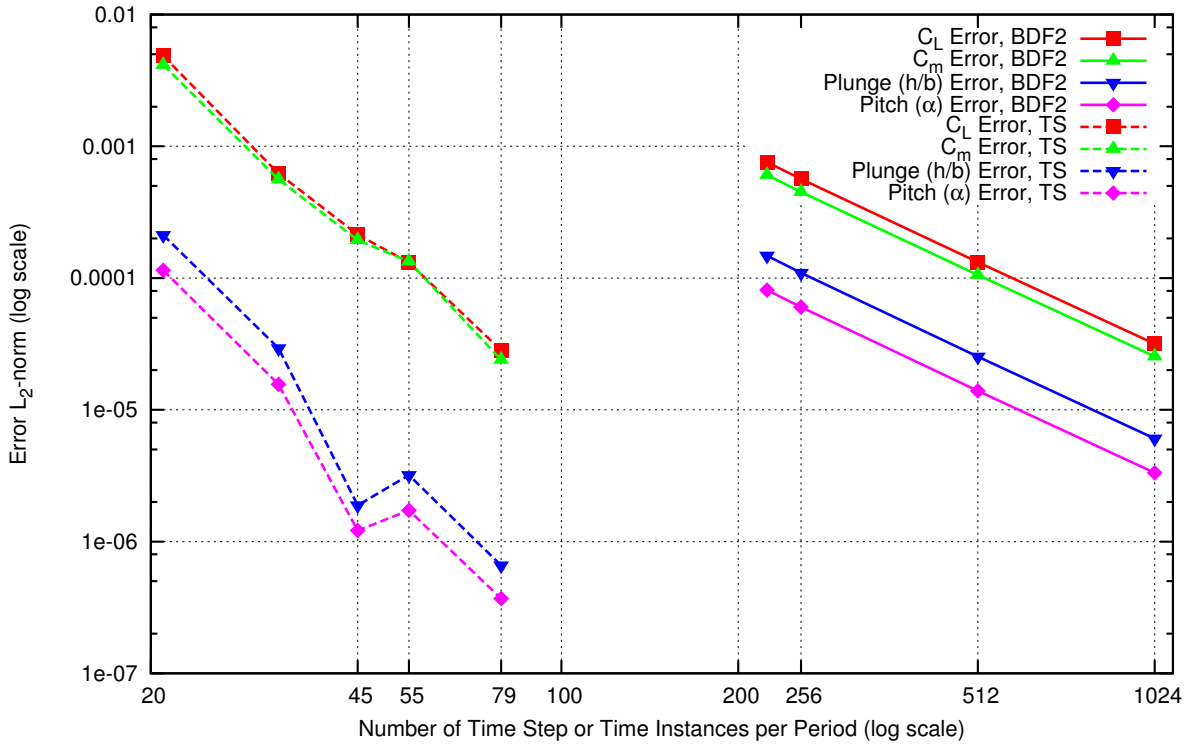

Fig. 27: Aeroelastic, fixed wing gust error, gust profile A (short gust), for BDF2 and TS methods with varying numbers of time steps and instances
($M_\infty = 0.75, V_f = 0.25$; 224, 256, 512, and 1024 time steps and 21, 33, 45, 55, and 79 time instances per period)